Review

Emerging Technologies to Image Tissue Metabolism

Vasilis Ntziachristos[1, 2, *]

v.ntziachristos@tum.de

Miguel A. Pleitez[1, 2]

Silvio Aime[3]

Kevin M. Brindle[4, 5]

[1]Institute of Biological and Medical Imaging, Helmholtz Zentrum München, Neuherberg 85764, Germany

[2]Chair of Biological Imaging, TranslaTUM, Technical University of Munich, Ismaningerstr. 22, Munich 81675, Germany

[3]Molecular Imaging Center, Department of Molecular Biotechnologies and Health Sciences, University of Turin, Turin 10126, Italy

[4]Department of Biochemistry, University of Cambridge, Old Addenbrooke's Site, Cambridge CB2 1GA, UK

[5]Cancer Research UK Cambridge Institute, University of Cambridge, Li Ka Shing Centre, Robinson Way, Cambridge CB2 0RE, UK

[*]Corresponding author

Due to the implication of altered metabolism in a large spectrum of tissue function and disease, assessment of metabolic processes becomes essential in managing health. In this regard, imaging can play a critical role in allowing observation of biochemical and physiological processes. Nuclear imaging methods, in particular positron emission tomography, have been widely employed for imaging metabolism but are mainly limited by the use of ionizing radiation and the sensing of only one parameter at each scanning session. Observations in healthy individuals or longitudinal studies of disease could markedly benefit from non-ionizing, multi-parameter imaging methods. We therefore focus this review on progress with the non-ionizing radiation methods of MRI, hyperpolarized magnetic resonance and magnetic resonance spectroscopy, chemical exchange saturation transfer, and emerging optoacoustic (photoacoustic) imaging. We also briefly discuss the role of nuclear and optical imaging methods for research and clinical protocols.

Ntziachristos et al. comprehensively review the state of the art in imaging metabolic processes in living tissues using non-ionizing radiation, including emerging methods based on magnetic resonance, optics, and optoacoustics (photoacoustics). These technologies uniquely allow for longitudinal studies of biochemical and physiological processes and can enhance the detection and assessment of metabolic diseases.

Main Text

Introduction

Imaging of tissue metabolism requires methods that sense tissue biochemistry and physiology, either through direct sensing of metabolites or by measuring processes that relate to metabolism. Nuclear imaging methods label specific molecules with radioactivity. Therefore, they present an excellent modality for the non-invasive assessment of metabolites and tissue function. Positron emission tomography (PET) offers high molecular specificity and sensitivity in imaging glucose uptake, amino acids, fatty acids, or carbohydrates (Lewis et al., 2015; Paulus et al., 2017), positioning PET as a ubiquitous tool for energy utilization. Despite its far-reaching abilities, the use of radioactivity and fast signal loss through radio-decay limit PET to applications where the benefits outweigh the risks; i.e., in detection of life-threatening diseases such as cancer and cancer metastasis or critical cardiovascular conditions. The use of ionizing radiation also reduces possibilities for repeated or longitudinal imaging; for example, in studies ranging from exercise physiology to understanding personalized metabolic parameters associated with environmental factors or

individual lifestyle.

Radioactivity-free methods based on nuclear magnetic resonance (NMR) have been employed as a prime tool in visualizing not only human morphology but also sensing tissue biochemical parameters. MRI is used to visualize pathophysiology changes in response to altered metabolism and can also detect lipids in tissues and separate them from water contributions. Moreover, localized spectroscopic imaging methods measure NMR spectra from specific volumes within tissue and reveal biochemical information in a spatially dependent manner, measuring concentrations of metabolites at select tissue locations. By changing the frequency of excitation and observation, ^{31}P-metabolites, such as phosphocreatine, ATP, or other ^{13}C-based organic molecules can be observed. Nevertheless, a major limitation of NMR methods is the low sensitivity achieved. Correspondingly, significant attention has recently been placed on methods that increase the signal-to-noise ratio in the detection of metabolites at physiological concentrations. Two of these approaches, dynamic nuclear polarization (DNP, also called hyperpolarized MRI) and chemical exchange saturation transfer (CEST), have changed the landscape of NMR sensing of tissue metabolism. As a complement to radiological methods that do not use ionizing radiation, optoacoustic imaging (also known as photoacoustic imaging) offers new capabilities for imaging metabolism. Optoacoustic technology enables portable label-free visualization of physiological parameters associated with metabolic processes, in particular label-free sensing of oxygen utilization through recording oxygenated and deoxygenated hemoglobin gradients. In contrast to older attempts using near-infrared spectroscopy and imaging, optoacoustic imaging brings unique cross-sectional imaging performance that provides resolution and quantification at least an order of magnitude greater than other optical methods.

We review herein technologies that allow non-invasive metabolic imaging in animals and humans. We briefly discuss nuclear imaging methods and their impact on assessing disease metabolism but emphasize methods that employ non-ionizing energies and are possibly better suited for repeated, longitudinal imaging in patients and volunteers. Longitudinal imaging can enable studies aiming to resolve basic tissue function and responses to lifestyle, nutritional and environmental influences, or in relation to chronic diseases. These methods therefore qualify not only for disease diagnostics in cancer or cardiovascular disease but also as tools employed to understand physiological conditions associated with individualized phenotypes or disease progression.

Nuclear Imaging

Radionuclide imaging offers a direct way to visualize biomolecules in tissue, by radioactively labeling specific metabolites. The labeled molecules are administered into the body and their spatial localization is tracked with a tomographic imaging system that is sensitive to the high-energy rays emitted; i.e., it can detect gamma rays emitted directly from the label (single photon emission) or record pairs of gamma rays produced by positron emission and annihilation (positron emission). Nuclear imaging methods have demonstrated broad abilities for imaging metabolism in cancer, cardiovascular disease, neuronal function and neurodegeneration, diabetes, or inflammation. The best known method is the visualization of glucose uptake with PET using the glucose analog 2-deoxy-2-[^{18}F]fluoro-D-glucose (FDG). FDG-PET is widely employed for detecting cancer and metastatic lesions; identifying tissue viability in ischemic myocardia; or characterizing metabolic profiles of tissues in obesity, diabetes, or brain function (Labbé et al., 2012; Lewis et al., 2015; Osborn et al., 2017). Imaging of glucose uptake has also been considered with other agents; for example, ^{11}C-glucose, which has been shown to offer more accurate measurements of myocardial glucose uptake compared with FDG but with a shorter half-life (~20 min versus ~110 min for FDG) and more complex synthesis (Gropler, 2010).

Development of many other tracers has given PET broad abilities to study metabolism. For example, fatty acid utilization has been considered using 14-(*R*,*S*)-[^{18}F]fluoro-6-thiaheptadecanoic acid (FTHA) or, more recently, 16-[^{18}F]fluoro-4-thia-palmitate (FTP), agents employed for imaging myocardial β-oxidation or brown fat activity (Bauwens et al., 2014; DeGrado et al., 2010; Pandey et al., 2011). ^{11}C-acetate has been used for measuring myocardial oxygen consumption (MVO_2) or membrane lipid synthesis in cancer (Grassi et al., 2012). ^{15}O-oxygen and ^{11}C-palmitate have been used to measure MVO_2 and overall oxidative metabolism (Geltman, 1994; Karamitsos et al., 2010; Li et al., 2015; Muzik et al., 2013). Preliminary studies with ^{11}C-lactate have also shown potential to visualize lactate oxidation. Likewise ^{11}C-choline or ^{18}F-fluorocholine have been considered in imaging metastatic tumors and several types of cancer, in particular cancers of the prostate, lung, esophagus, and brain (Plathow and Weber, 2008; Wieder et al., 2017). ^{18}F-glutamine has been used to monitor metabolism in gliomas (Venneti et al., 2015).

PET abilities are complemented with single-photon emission computer tomography (SPECT), which has also been considered for studying fatty acid metabolism using 15-(P-iodophenyl)-pentadecanoic acid and branched-chain analogs such as ^{123}I-β-methyl-P-iodophenylpentadecanoic acid, with the latter exhibiting better characteristics for imaging. SPECT has high sensitivity, and the long half-life of SPECT radiotracers is also advantageous. Classic agents such as Tc-99m-labeled polyphosphonates or Tc-99m-pertechnetate can also be considered as targeting metabolically active areas. Nevertheless, limitations in quantification accuracy associated with the unfavorable spatial and temporal resolution generally make PET a preferred imaging modality (Gropler, 2010).

Nuclear imaging methods offer great potential for imaging various aspects of complex metabolism cycles and their perturbations as they associate with different metabolic conditions. Nevertheless, access to longitudinal studies becomes challenging due to the infrastructure required for radiotracer production and, importantly, the use of radioactivity limits use in repeated imaging sessions. For this reason, we have devoted only a brief mention to nuclear medicine methods herein, and instead focus on imaging methods that do not require ionizing radiation.

The Optical Method: Advances in Optoacoustic Imaging

Macroscopic optical imaging of tissues is occasionally considered an alternative to nuclear imaging. The use of fluorescent agents or bioluminescence offers molecular imaging abilities that resemble those of nuclear imaging methods. Nevertheless, while a multitude of fluorescence agents have been developed for cancer, cardiovascular, or neurodegenerative imaging, only a few pilot studies and agents have been reported for imaging metabolism (Henkin et al., 2012; Kovar et al., 2009).

Moreover, the operational characteristics of optical and nuclear imaging vary significantly. In contrast to nuclear imaging, conventional fluorescence and bioluminescence imaging yields two-dimensional images of surface-weighted signals; i.e., signals detected from superficial fluorescence activity. Tomographic methods, such as fluorescence molecular tomography (FMT) (Ale et al., 2012; Ntziachristos et al., 2002), yield three-dimensional images of low resolution, which is due to photon diffusion. Optical methods in general and FMT in particular are also limited by the fact that they do not reach the penetration depth achieved by high-energy photons. Typical penetration depths for FMT are within the 2–10 cm range, depending on the optical attenuation of the organ studied.

Sensing of muscle activity and hemodynamics has been also pursued since the 1990s using near-infrared spectroscopy. The technique illuminates tissues with near-infrared light at different wavelengths and detects changes in the intensity or other parameters of this light after it has propagated for a few millimeters to centimeters through tissue. In the course of propagation through tissue, near-infrared light is modified by the optical properties of the tissue, and it contains information on hemoglobin absorption and scattering. Consequently, near-infrared spectroscopy was developed to record hemoglobin in muscle and other tissues and yield information on tissue oxygenation by quantifying the relative concentrations of oxygenated and deoxygenated hemoglobin (Boezeman et al., 2016; Perrey and Ferrari, 2018). However, the strong photon diffusion and the coupled influence of tissue absorption and scattering on the optical measurement yields an ill-posed mathematical problem that complicates efforts to reach accurate solutions. Attempts to increase the number of measurements from a few optodes to a large number of measurements and the use of light of modulated intensity improves quantification but nevertheless has not yet yielded sufficient performance to allow disseminated use of this method in research or clinical applications.

The emergence of optoacoustic methods shifts the paradigm of the optical method, in particular diffuse optical imaging and spectroscopy methods, allowing three-dimensional high-resolution optical imaging inside tissue. While the penetration depth is similar to that of diffuse optical tomography methods (Ntziachristos, 2010), the high spatial resolution achieved allows quantification ability and image fidelity never before available to optical imaging (Mohajerani et al., 2015), yielding new abilities for metabolic imaging. The improvement in quantification results from the fact that the inversion problem in optoacoustic imaging is better posed than in diffuse optical methods, leading to a fundamentally more accurate mathematical solution after inversion. Moreover, by resolving smaller voxel sizes, optoacoustic imaging is less prone to partial volume effects compared with diffuse optical methods.

Recently, many of the limitations of diffuse optical bio-sensing and imaging have been overcome using optoacoustics (Longo et al., 2017; Taruttis and Ntziachristos, 2015). Optoacoustic imaging at a single wavelength enables detailed morphological imaging of vasculature, organs, and other structures that absorb light at the wavelength employed. Illumination at multiple wavelengths resolves images with spectral information, which can be employed to unmix different chromophores in tissue, based on their spectral signatures, including hemoglobins, water, and lipids (Taruttis and Ntziachristos, 2015). One key aspect in the quantification of chromophores in tissues relates to accounting for the effects of photon fluence in tissues. Tissue attenuates light at a different rate depending on wavelength. Therefore, the apparent spectrum of a chromophore changes depending on its depth and the surrounding tissue optical properties, an effect termed spectral coloring (Tzoumas et al., 2016). Recently a method based on eigenvalue separation of spectral contributions of tissues has been introduced to account for the effects of spectral coloring by converting the spectral unmixing problem from the spatial to the spectral domain (Tzoumas et al., 2016). The method has shown superior quantification ability with depth, compared with linear unmixing methods.

In parallel, powerful emerging microscopy methods allow the study of metabolic processes at the cellular and subcellular levels that were never possible in the past. On many occasions, these methods sense metabolic parameters in label-free mode; i.e., without the use of contrast agents. In the following sections, we explain the main abilities of optoacoustic imaging and its applications in imaging metabolism.

Principles

Optoacoustic imaging dates back to the 1970s but has seen significant progress in the past decade, moving beyond laboratory prototypes into clinical applications (Knieling et al., 2017; Reber et al., 2018; Stoffels et al., 2015). The method illuminates tissue using light of transient intensity. A common implementation is using photon pulses in the nanosecond range. Pulses of several tens of millijoules are required for reaching multi-centimeter depths. The transient mode of the energy employed stimulates the generation of ultrasound waves from photon-absorbing moieties due to thermo-elastic expansion. The nanosecond pulses of light propagate diffusively in tissue and excite ultrasound waves volumetrically from all sites of optical absorption that are sufficiently illuminated. Ultrasound detectors record in this case time-resolved pressure signals at the tissue boundary (Figure 1A). Using tomographic techniques, detection of tissue cross-sections can be achieved in real time, using multi-element transducers, in analogy to ultrasonography. The use of ultrasound detection for resolving optical absorption allows image formation based on principles of ultrasonic diffraction and not photon scatter, thus significantly improving the resolution of the optical images over conventional optical imaging methods. The optoacoustic signals generated using ultrafast pulses contain a broader spectrum of ultrasonic frequencies compared with the ones employed in ultrasound imaging. The optoacoustic frequency spectrum is best detected by broadband ultrasound detectors in order to achieve high image quality.

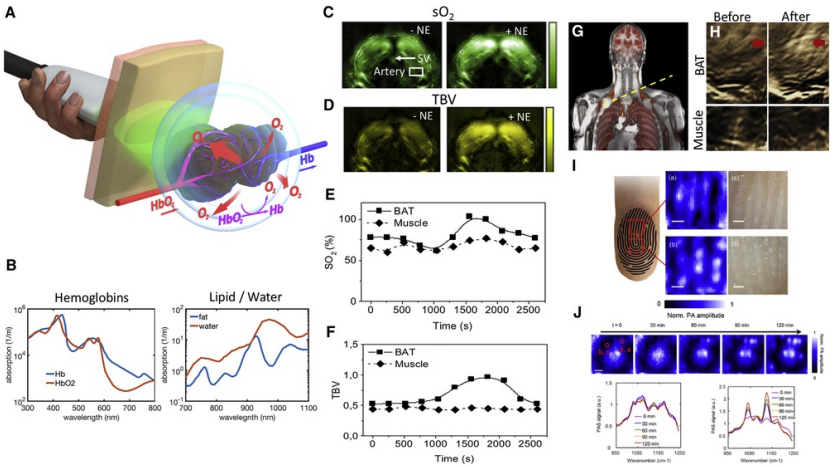

Figure 1 Imaging of Metabolism with MSOT and Microscopy

(A) General schematic representation of optoacoustic metabolic imaging. Tissue is illuminated with a short-pulse laser that penetrates for several millimeters to centimeters depending on pulse energy and wavelength. Areas that contain optical absorbers, such as hemoglobins or lipids, absorb and then convert the light energy to acoustic waves due to thermoelastic expansion. The generated acoustic signal is detected by an ultrasound sensor (or sensor array), in this case integrated into the excitation head, and the signal is later used for spatiotemporal reconstruction of the light-absorbing/sound-emitting structures depending on molecular concentration. For instance, imaging of oxy- and deoxyhemoglobin can be used to analyze the gradients of oxygen consumption in tissue.

(B) Optical absorption spectra of key biomolecules used as contrast sources for imaging metabolism. (Left) Spectra of deoxyhemoglobin (Hb) and oxyhemoglobin (HbO_2). (Right) Spectra of water and lipids.

(C–F) Assessment of blood sO_2 and TBV before and after activation of inguinal brown adipose tissue (iBAT) with NE in mice. (C) Multispectral optoacoustic images of sO_2 before and after injection of NE. (D) Multispectral optoacoustic images of TBV before and after injection of NE. (E) Time course of sO_2 in iBAT and muscle. (F) Time course of TBV in iBAT and muscle.

(G and H) *In vivo* assessment of BAT metabolism in humans by handheld optoacoustic tomography. (G) Coronal MRI-positron emission tomography of the upper torso of a volunteer used for co-registration. The imaging plane used for MSOT is indicated by the dotted yellow line. (H) MSOT was used to image BAT (red arrows) and muscle areas before and after cold activation.

(I and J) *In vivo* mid-infrared microscopy for monitoring intracutaneous glucose in humans. (I) Mid-infrared micrographs at two selected areas on the index finger. Scale bars, 250 μm. (J) Spectral imaging monitoring of human skin at selected sections during sweat secretion. This information was used to discriminate a suitable measuring spot for glucose monitoring on skin. Scale bars, 250 μm.

(B) Prepared using data from https://omlc.org/spectra/ (visited in March 2018). (C–H) Reproduced from Reber et al. (2018) with permission. (I and J) Reproduced from Sim et al. (2018) with permission.

Different geometrical configurations and detector features such as the bandwidth of operation and geometrical characteristics allow operation at different scales. For human imaging, frequencies in the range of 0.1–10 MHz are typically employed using multi-element array transducers, enabling imaging through a few centimeters of depth with 100–500 μm resolution (typically 200–300 μm). Curved detectors (i.e., detectors that arrange multiple elements on an arc geometry) achieve better axial resolution, leading to images of higher fidelity compared with linear detectors used in conventional ultrasonography (Dima et al., 2014). Implementations at higher frequencies and different geometries, such as raster scan mesoscopy or microscopy implementations, can also be employed depending on the application (Aguirre et al., 2017). While single-element detection scanning approaches delay acquisition because an image is formed by scanning pixel by pixel, clinical systems based on multi-element array transducers can detect a complete two-dimensional or three-dimensional image in a single snapshot, achieving fast operation analogous to ultrasonography.

Particular progress with fast-tuning lasers has enabled acquisition of spectral images at video rates, recently allowing the clinical propagation of the technology. Current multi-spectral optoacoustic tomography (MSOT) systems employed in clinical studies may utilize up to 50 frames per second; each frame is acquired at a different wavelength (Taruttis and Ntziachristos, 2015). It has been shown that, despite the speed achieved by modern laser technologies, algorithmic processing of subsequent frames can minimize motion effects present in the images collected at different wavelengths (Taruttis et al., 2012). A critical further component is the analysis of multi-spectral data to accurately resolve images of different chromophore distributions in tissue. New algorithms account for the effects of wavelength-dependent light fluence attenuation in tissue and improve on spectral coloring artifacts and detection sensitivity.

Applications

Spectral optoacoustics detects and separates oxygenated and deoxygenated hemoglobins, myoglobins, lipids, water, and other tissue optical absorbers, depending on the wavelength range employed. Oxy- and deoxyhemoglobin absorb strongly in the visible range and can therefore be visualized with high contrast. However, penetration depths cannot exceed 1–2 mm for light with wavelengths in the visible range due to strong light attenuation. The near-infrared region at 650–1,000 nm offers a

balance between contrast and depth achieved and is preferred for visualizing hemodynamics deeper in tissues, down to a few centimeters deep. Beyond the 900 nm range, optical attenuation is dominated by lipids and water. MSOT becomes sensitive to lipids and water in the 900–1,000 nm region, with lipids exhibiting a characteristic peak at 930 nm and water at 950 nm (Figure 1B). In analogy to hemoglobins in the visible region, rising lipid and water absorption at wavelengths beyond 1 μm limits the penetration depth of the optoacoustic method but improves the sensitivity and contrast at superficial depths.

MSOT recently demonstrated different label-free clinical imaging applications, spanning from non-invasive imaging of inflammation in Crohn disease patients (Knieling et al., 2017) or psoriasis patients (Aguirre et al., 2017) to breast cancer imaging (Diot et al., 2017) and detection of metastatic melanoma (Stoffels et al., 2015). The ability of MSOT to image metabolism label-free is based on detection of hemoglobin as an intrinsic tissue biomarker of oxygen. When hemoglobin binds oxygen, its spectrum changes (Figure 1B) and this change can be detected by spectral optoacoustics. Then oxygen utilization, indicative of metabolic rate, can be computed as the rate of change from oxygenated to deoxygenated hemoglobin; i.e., gradients of tissue oxygenation in space or time.

Recently it was shown that MSOT-resolved hemoglobin gradients accurately revealed metabolic changes in activated brown adipose tissue (BAT) in animals and humans, and these changes were confirmed by indirect calorimetry (Reber et al., 2018). In mice, BAT activation was induced by norepinephrine (NE) administration. MSOT showed that NE altered hemoglobin levels only in the brown fat, not in surrounding muscle or other soft tissues, and it triggered changes in the levels of oxy- and deoxyhemoglobin that were consistent with oxygen consumption as measured using indirect calorimetry of the gases breathed out by the animal (Figures 1C–1F). In humans, cold exposure significantly increased levels of oxy- and deoxyhemoglobin and therefore total blood volume (TBV) in the subclavicular brown fat depots but not in neighboring muscle. MSOT separation of oxy- and deoxyhemoglobin allowed the computation of high-resolution oxygen saturation (sO_2) and hemoglobin concentration (TBV) images acquired over time (Figures 1G and 1H). The images revealed dynamic characteristics of activation, showcasing novel possibilities for the label-free study of metabolic properties in tissue. The study proposed sO_2 as a marker of oxidative metabolism and TBV rates (time gradients) as a marker of blood volume influx (tissue perfusion).

MSOT also demonstrated imaging of BAT and beige adipose tissue morphology based on spectral (color) differences with white adipose tissue (WAT) (Reber et al., 2018). Brown fat is highly vascularized and takes its color from the greater abundance of mitochondria than in pale white or yellow WAT. Beige fat differs from BAT or WAT in mitochondrial content and lipid droplet size, giving it a different spectrum from WAT. These spectral changes can be captured by MSOT not only in the visible but also near-infrared spectrum. Spectral identification of BAT correlated well with the proton density fat fraction derived from MRI, although image co-registration protocols are needed for accurate comparison. Moreover, water and lipid tissue content captured by MSOT correlated with MRI measurements.

Similar calculations could be performed in exercising muscle (Diot et al., 2015), identifying MSOT as a ubiquitous tool for studying hemodynamics and oxygen consumption in tissue. Overall, optoacoustic tomography can be applied for two- or three-dimensional imaging of tissue hemodynamics (Deán-Ben et al., 2017a, 2017b; Yao et al., 2015). Moreover, using a ring-shaped optoacoustic tomography system, it was possible to image both anatomy and glucose uptake in a single modality (Chatni et al., 2012). Anatomical information was obtained from the endogenous contrast of hemoglobin, and glucose metabolism was imaged using dye-labeled 2-deoxyglucose in the near-infrared region.

As an alternative to the use of labels, it has also been shown that optoacoustic measurements can non-invasively capture glucose label free when combined with the chemical specificity of near-infrared or mid-infrared spectroscopy (Ghazaryan et al., 2018; Pleitez et al., 2013). Although these studies relied on single-point measurements, they indicate imaging potential, as recently demonstrated *in vivo* in human skin (Sim et al., 2018) (Figures 1I and 1J).

Concluding Remarks

Label-free MSOT can sense tissue metabolism using safe light illumination based on portable systems. Such ability can bring assessment of tissue function and lipid content to point-of-care sites, potentially offering a novel tool for disseminated measurement of metabolic conditions. By enabling longitudinal, point-of-care or even home-based measurements, MSOT could support investigations beyond the confines of radiology suites or the limitations of radio-isotope production and short lifetimes.

The use of hemoglobin as a tissue sensor of metabolism can be complemented by direct capture of water and lipid, expanding the application potential of the technique. Optoacoustic imaging could be potentially applied to a larger range of applications spanning exercise physiology, bio-energetic/obesity-related studies, and different metabolic diseases such as metabolic syndrome, mitochondrial diseases, and disorders of lipid metabolism. Compared with generic measurement approaches such as indirect calorimetry, MSOT can provide accurate observation in a spatially confined manner. Therefore, combination of MSOT with calorimetry studies can lead to high complementarity, whereby global metabolism and timing can be assessed in parallel to local measurements.

Nevertheless, *in vivo* MSOT is limited to penetration depths of 2–3 cm. Therefore, we anticipate its use primarily in small-animal research or specific human interrogations; for example, in studying superficial muscle energetics or systemic lipid metabolism at accessible tissue sites. Moreover, while generic physiological responses can be recorded in label-free mode, specific contrast at the cellular and subcellular levels may require appropriate optoacoustic agents, which will mean overcoming regulatory challenges. A possible interesting alternative is to conduct measurements in extended spectral regions, as discussed in the following section.

Optical Microscopy

Different forms of optical spectroscopy, including Raman or mid-infrared spectroscopy, can directly detect a number of metabolites, including glucose and lipids, based on their spectral fingerprints. These techniques are only

applicable to superficial measurements, since their penetration depth is limited to a few micrometers to hundreds of micrometers in tissue. Nevertheless, we briefly review this field as it relates to research investigations but also potentially to *in vivo* application through portable microscopes enabling intravital measurements.

Principles

Generally, modern microscopy strongly depends on contrast generation, such as the use of reporter genes (e.g., fluorescent proteins) or fluorescent dyes and targeted agents. Using agents for imaging metabolic cycles can bring challenges related to agent production, bio-distribution, specificity, or toxicity. A powerful alternative is the use of label-free dynamic imaging of biomolecules for direct metabolic imaging. Depending on the spectrum and technology, different metabolites and functional parameters can be detected. UV microscopy detects nucleic acids, proteins, and lipids at high spatial resolution but at the expense of cell damage due to elevated photo-toxicity; therefore, this technique is generally limited to tissues or *ex vivo* studies.

Naturally occurring FAD and NADH auto-fluorescence has long been employed for visualizing these metabolic coenzymes in label-free imaging. Recently such auto-fluorescence has been employed to monitor metabolic perturbations in glycolysis and glutaminolysis, mitochondrial uncoupling, and fatty acid oxidation and synthesis using two-photon microscopy (Liu et al., 2018). Nevertheless, auto-fluorescent contrast from cells is often weak and may not be specific in measurements from complex systems containing other naturally occurring fluorochromes.

Recently, vibrational spectroscopic imaging and microscopy have gained attention due to the molecular specificity achieved. Contrary to electronic transitions (excited by visible light), the vibrational modes of a molecule are determined by its spatial atomic configuration, strength of its chemical bonds, isotopic content, and interactions with surrounding and/or attached molecules. Therefore, vibrational contrast offers high chemical specificity in a label-free manner. Information about the vibrational state of a molecule can be obtained indirectly by inelastic Raman scattering, directly by excitation of fundamental vibrational modes with mid-infrared radiation, or by overtone-vibrational excitation by near-infrared absorption. These modalities differ in terms of operational characteristics such as the sensitivity, specificity, spatial resolution, imaging depth, imaging speed, and contrast portfolio achieved.

Coherent Raman scattering imaging can detect lipids, proteins, and nucleic acids in living cells and tissues at video rates and with sub-micrometer spatial resolution. As a result, such imaging can resolve subcellular structures (Cheng and Xie, 2015) (Figures 2A–2F). For instance, stimulated Raman scattering, which is a nonresonant background-free coherent Raman scattering modality in which the signal is directly proportional to the concentration, has been shown capable of functional imaging of label-free membrane potential and action potentials in neurons (Lee et al., 2017). This offers a powerful label-free alternative to genetically encoded calcium/voltage indicators. However, there is risk of photodamage, and the detection limit of Raman-based imaging is above 1 mM, as reported, for instance, when the source of contrast was the C–H bonds of phospholipids in cell membranes (Cheng and Xie, 2015; Potma and Xie, 2003) or the CH_3 bonds in dimethyl sulfoxide (Cheng and Xie, 2015; Wang et al., 2013). This detection limit poses a problem for label-free live-cell analytical imaging of other sources of biomolecular contrast present at lower concentrations, such as carbohydrates and proteins. Additionally, the intrinsic contrast portfolio of Raman imaging is incomplete. The spectral features of important carbohydrates, such as glucose or lactate, are too weak for live-cell imaging. For instance, glucose has been detected in living cells by stimulated Raman scattering, but only with the help of a labeled glucose analog that is metabolized under certain conditions (Hu et al., 2015). Other important bands, such as the amide II band of proteins, are also practically absent in Raman imaging.

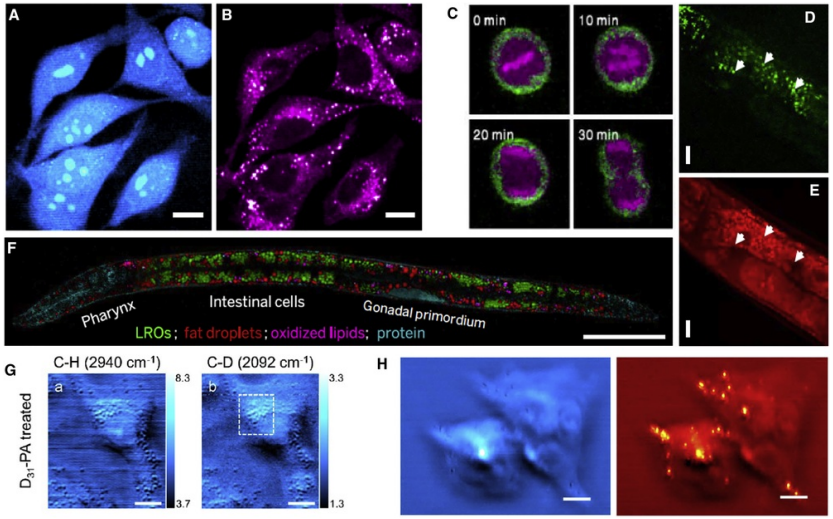

Figure 2 Direct Metabolic Imaging of Single Cells and Intact *C. elegans* with Vibrational Microscopy

(A-F) Metabolic imaging of single cells and intact *C. elegans* using stimulated Raman scattering microscopy. (A) Protein map of living HeLa cells with isotope labeling showing newly synthesized proteins. (B) Lipid map of the HeLa cells shown in (A). Scale bars in (A) and (B),

10 μm. (C) Time-lapse micrographs of DNA (magenta) and lipids (green) in a HeLa cell during cell division. (D) Cholesterol map of a living *C. elegans*. (E) Lipid map in living *C. elegans*. Scale bars in (D) and (E), 10 μm. (F) Chemical micrographs of living *C. elegans* showing lysosome-related organelles (LROs, green), neutral fat droplets (red), oxidized lipids (magenta), and proteins (cyan). Scale bar, 50 μm.

(G and H) Metabolic imaging of single cells using mid-infrared photothermal microscopy. (G) Micrographs of fatty acid metabolites (left) and lipids/proteins (right) in A549 lung cancer cells treated with D_{31}-palmitic acid. Scale bars, 10 μm. (H) Micrographs of MIA PaCa-2 cells treated with the lipid inhibitor JZL184 showing distributions of lipids (left) and JZL184 (right). Scale bars, 20 μm.

(A–F) Reproduced from Cheng and Xie (2015) with permission. (G) Reproduced from Zhang et al. (2016) with permission. (H) Reproduced from Bai et al. (2017) with permission.

Contrary to Raman spectroscopy, mid-infrared imaging/spectroscopy is a direct vibrational modality offering cross-sections up to eight orders of magnitude larger, which can therefore provide higher sensitivity. For instance, the secondary structure of proteins at concentrations as low as 3.6 μM (or 0.25 mg/mL) has been analyzed thanks to enabling technologies such as quantum cascade lasers (Schwaighofer et al., 2016). In clinical applications, mid-infrared microspectroscopy has shown potential for fast quantitative cancer diagnosis based on histological samples, without major disturbance to the routine pathology workflow (Baker et al., 2014). Additionally, the sensitivity and specificity of mid-infrared spectroscopy have proven adequate for non-invasive label-free glucose monitoring in human epidermis when combined with excitation by a quantum cascade laser and optoacoustic or photothermal detection (Pleitez et al., 2013, 2015; Sim et al., 2018). However, because of the strong absorption of mid-infrared radiation by water, applying mid-infrared microscopy to live-cell or tissue imaging requires confining cells within cuvettes about 10 μm thick in order to reduce the column of water. Such confinement prevents normal cellular proliferation and behavior; as a result, mid-infrared live-cell microscopy has not been broadly implemented. Another limitation of mid-infrared microscopy is its low spatial resolution due to the long wavelengths used (from 2.5 to 16 μm). To overcome this limitation, the combination of a mid-infrared pump and a visible probe using the photothermal effect has been proposed and has demonstrated great potential (Bai et al., 2017; Lee and Lee, 2011; Zhang et al., 2016) (Figures 2G and 2H). Nevertheless, although mid-infrared photothermal images of living cells and *Caenorhabditis elegans* have been reported with optical resolution in the visible wavelength range, the contrast and overall image quality are still much lower than what can be expected from the strong mid-infrared absorption by biomolecules.

Applications

The ability to directly observe chemical bonds of biomolecules offers an interesting modality for the assessment of metabolic processes. By monitoring the vibrations of the C–H bonds in the hydrophobic tails of lipids as well as vibrations of the C–D bonds of deuterated glucose, for instance, it was possible to observe glucose/lipid metabolism during *de novo* lipogenesis in pancreatic and prostate cancer cells by means of stimulated Raman scattering (Li and Cheng, 2014). A similar approach, using deuterated amino acids, was applied for monitoring the synthesis of proteins in living HeLa, HEK293T, and neuron-like N2A cells (Wei et al., 2013). Beyond the use of isotopic labeling, it recently became possible to directly monitor lipid/protein dynamics during lipolysis in brown and white adipocytes in a label-free manner using a combination of mid-infrared excitation and optoacoustic detection (Pleitez et al., 2018). Vibrational microscopy has also been used to observe metabolic activity in small-animal models. For instance, in *C. elegans*, a combination of hyperspectral stimulated Raman scattering imaging and multivariate analysis in the fingerprint region allowed the quantitative mapping of fat distribution, degree of fat unsaturation, lipid oxidation, and cholesterol storage in the whole animal (Wang et al., 2014).

Concluding Remarks

Molecular vibration imaging has enormously extended the range of possibilities for label-free metabolic imaging, but many challenges lie ahead. While Raman imaging has superior resolution, mid-infrared imaging promises the strongest sensitivity and full coverage of biomolecular contrast. However, when it comes to label-free imaging in depth, the near-infrared range is the weapon of choice, especially when combined with optoacoustic sensing.

Magnetic Resonance

MRI typically acquires signal from tissue water protons to create relatively high-resolution images of tissue anatomy. The NMR relaxation properties of these protons are a source of image contrast and make MRI an ideal technique for imaging soft tissues. Metabolic information can be obtained from these images if changes in perfusion or tissue metabolism result in changes in blood oxygenation; for example, in the brain (Raichle, 2001) or in tumors (Padhani et al., 2007). Deoxygenated hemoglobin, which is paramagnetic, increases the relaxation rate of water protons and can result in decreased image signal intensity.

Direct detection of tissue metabolism requires magnetic resonance spectroscopy (MRS), which has been employed for several decades for this purpose. Spectroscopic information can be obtained with reference to the magnetic resonance images, in which case the technique is termed localized spectroscopy. With appropriate sequences, spectroscopic information can be recorded from well-defined voxels in the tissue, therefore accurately relating spatial information to spectral information.

^{31}P-MRS ~~has been~~was used in early studies to interrogate tissue bioenergetics (reviewed in Gadian and Radda, 1981) and translated to the clinic in 1981 (Ross et al., 1981). ^{1}H MRS has developed from cell studies in the late 1970s (Brindle and Campbell, 1984) to become a widely, although not routinely, used tool today. For example, it has been used to distinguish benign from malignant lesions in the prostate (Kurhanewicz et al., 2002) and to characterize brain tumors (Howe et al., 2003). Protons can be detected with relatively high sensitivity compared with other nuclei, but ^{1}H spectra provide only a profile of cellular metabolites at a particular point in time. There is no information about

metabolic flux unless (1) there are time-dependent changes in cellular metabolites resulting from a change in state of the tissue (e.g., when a muscle starts to contract or a tumor becomes hypoxic); and (2) a series of spectra is acquired. However, if the tissue is in a particular biological state, then the metabolites are usually in a steady state, such that their rate of synthesis equals their rate of breakdown and their concentrations are time invariant. In order to obtain information about metabolic flux under these circumstances, we need to introduce an isotopically labeled substrate; in the case of MRS, this typically means a ^{13}C-labeled substrate, although in early studies with ^{1}H-MRS, deuterium-labeled substrates were also used (Brindle et al., 1982b). The application of ^{13}C-MRS to biological systems was pioneered by Shulman's group (Avison et al., 1986) (Figures 3A–3C). Introduction of a ^{13}C-labeled substrate, for example ^{13}C-labeled glucose, results in time-dependent changes in the labeling of cell metabolites, where these changes can be detected *in vivo* with non-invasive ^{13}C-MRS measurements. However, the much lower sensitivity of ^{13}C to magnetic resonance detection means that imaging is not possible. Nevertheless, this technique has been translated to the clinic; for example, to measure muscle glycogen synthesis following infusion of ^{13}C-labeled glucose (Shulman et al., 1990). Sensitivity can be improved by indirect detection of the ^{13}C label through spin-coupled protons, although temporal and spatial resolution are still relatively poor (Brindle et al., 1982a; Rothman et al., 1985). Magnetic resonance measurement of metabolic fluxes using ^{13}C-labeled substrates was revolutionized in the early 2000s by the introduction of dissolution DNP, which can increase the sensitivity of detection of ^{13}C-labeled molecules by >10^4-fold (Ardenkjaer-Larsen et al., 2003), enabling real-time imaging of metabolic fluxes *in vivo* (Golman et al., 2006). There have been several recent and comprehensive reviews of this technique (Brindle, 2015; Comment and Merritt, 2014; Keshari and Wilson, 2014), and therefore we will discuss here newer developments, focusing on studies in cancer, where most of the work has been done to date. There have, however, also been studies in other biological systems, notably the heart (Cunningham et al., 2016), reviewed in Rider and Tyler (2013).

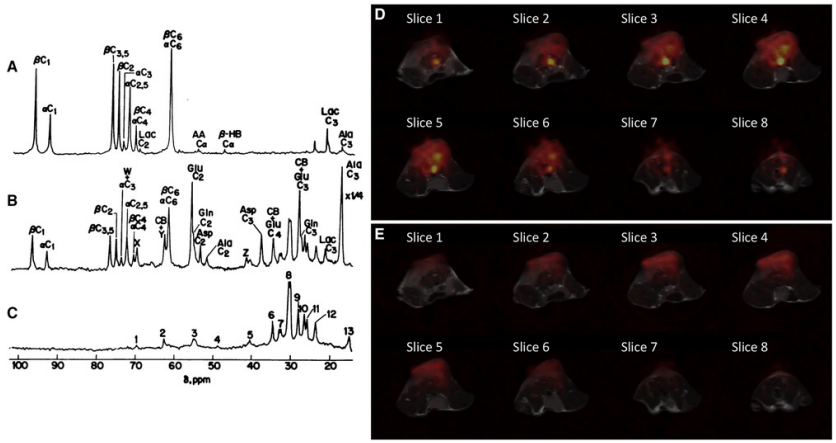

Figure 3 Imaging of Metabolism with Magnetic Resonance

(A–C) ^{13}C spectra from a perfused mouse liver. The liver was infused with [3-^{13}C]alanine and spectra were acquired at (A) 240 min and (B) 150–180 min. Each spectrum took 41 min to acquire. The spectrum in (C) shows natural abundance ^{13}C signal acquired before the labeled alanine was infused. Each peak represents an individual carbon atom in the indicated molecule: βC_1, αC_1, $\beta C_{3,5}$, βC_2, αC_3, $\alpha C_{2,5}$, αC_4, βC_6, and αC_6 refer to carbons of the glucose anomers. Glu C_2, glutamate C2; Gln C_2, glutamine C2; Asp C_2, aspartate C2; Ala C_2, alanine C2 Lac C_3, lactate C3; AA Cα, acetoacetate CH_2; and β-HB Cα, β-hydroxybutyrate CH_2.

(D and E) Images of (D) [1-^{13}C]pyruvate and (E) [1-^{13}C]lactate, acquired at 14 s (pyruvate) and 15 s (lactate) after intravenous injection of hyperpolarized [1-^{13}C]pyruvate into a tumor-bearing mouse. Images were overlaid on a T_2-weighted ^{1}H image of tissue water. The implanted tumor is visible at the top of individual images. Each set of images was acquired in <125 ms.

(A–C) Reproduced from Cohen et al. (1979) with permission. (D and E) Reproduced from Wang et al. (2017) with permission.

Principles

When a spin ½ nucleus, such as ^{1}H or ^{13}C, is placed in a strong magnetic field, the spins adopt one of two allowed energy levels, with a slight excess of spins in the lower energy level. The population difference between these energy levels shows a Boltzmann distribution,

$$\frac{N_{upper}}{N_{lower}} = e^{-\Delta E/kT} \qquad \textbf{(Equation 1)}$$

where N_{upper} and N_{lower} are the populations of the upper and lower energy levels, ΔE is the energy difference, k is the Boltzmann constant, and T is absolute temperature. There is only a slight excess of spins in the lower energy level; for example, at 37°C and a field strength of 1.5 T, which is typical for clinical scanners, there are only 5 ppm excess ^{1}H spins and only 1 ppm excess ^{13}C spins in the lower energy level. Since it is this population difference that gives rise to the magnetic resonance signal,

the technique is very insensitive. Typically, magnetic resonance signal is increased by using higher-field magnets, increasing the ΔE term in Equation 1 and thus the population difference between the two energy levels. However, it is evident from Equation 1 that the population difference is also inversely dependent on temperature, and therefore the population difference and magnetic resonance signal can also be increased by lowering the temperature. The problem with this approach is that the temperature must fall nearly to absolute zero before there is substantial nuclear spin polarization, which is clearly not feasible in an intact biological system. This “brute force” method is technically difficult, and it can take considerable time for nuclei to reach a polarized spin state (Hirsch et al., 2015).

In DNP, the ^{13}C-labeled molecule to be polarized (other magnetic resonance-active nuclei can also be polarized) is mixed with a stable radical, rapidly frozen to form a glass, and then placed in a strong magnetic field (typically 3–9 T) at ~1.2 K. This low temperature can be achieved relatively easily by boiling off liquid helium under vacuum. At this temperature the spins of the unpaired electrons on the radical are almost completely polarized. The electron spin polarization can then be transferred to the ^{13}C spins by microwave irradiation near the electron spin resonance frequency, which typically takes ~1 hr, depending on the nucleus and molecule to be polarized. The key development, introduced by Golman, Ardenkjaer-Larsen and colleagues in the early 2000s, was the dissolution process, in which the sample is heated rapidly to body temperature with substantial retention of the nuclear spin polarization (Ardenkjaer-Larsen et al., 2003). The hyperpolarized ^{13}C-labeled substrate can then be injected into the biological system under study, and a series of spectra or spectroscopic images can be acquired to follow redistribution of the ^{13}C label among cellular metabolites. The limitations of the technique include the short lifetime of the polarization, which decays with a time constant given by the T_1 of the ^{13}C nucleus. For [1-^{13}C]pyruvate, a widely used substrate, the T_1 *in vivo* is only 20–30 s, which means that it must reach the target tissue and undergo significant metabolism within tens of seconds and that images must be acquired within 2–3 min. This limits the substrates that can be studied to those that show fast cell uptake and rapid subsequent metabolism and has necessitated the development of very fast spectroscopic imaging techniques (Geraghty et al., 2017; Hurd et al., 2012; Josan et al., 2014; Schmidt et al., 2014; Shin et al., 2015; Wang et al., 2017) (Figures 3D and 3E). The ^{13}C polarization lifetime can be extended by deuterating the molecule; for example, perdeuteration of uniformly labeled glucose extended the T_1s of some resonances from ~1 s to 10 s, allowing imaging of label flux through all 10 steps of the glycolytic pathway (Rodrigues et al., 2014). The polarized substrate is diluted during the dissolution process and therefore the original solution must be very concentrated, limiting application of the technique to highly soluble molecules that will form a glass when rapidly frozen.

Despite these limitations, numerous hyperpolarized substrates have been polarized and studied *in vivo* (Brindle, 2015; Comment and Merritt, 2014; Keshari and Wilson, 2014). The substrate [1-^{13}C]pyruvate has been translated to the clinic, where it has been used to study both tumors (Aggarwal et al., 2017; Miloushev et al., 2018; Nelson et al., 2013) and heart muscle (Cunningham et al., 2016). Current efforts to improve the polarization process include working at higher magnetic fields and lower temperatures, which increases the level of spin polarization (Hurd et al., 2012); another approach is first to polarize protons in the ^{13}C-labeled molecule and then to transfer polarization to the ^{13}C nucleus, which speeds up the polarization process (Bornet et al., 2013). The liquid state polarization of the substrate injected into the biological system can also be improved by using a pump system to ensure rapid transfer from the polarizer (Cheng et al., 2013; Mishkovsky et al., 2017). Signal from a hyperpolarized ^{13}C-labeled substrate can be further increased by transferring the polarization to adjacent spin-coupled proton spins, which, because of a nearly 4-fold higher gyromagnetic ratio, have four times the magnetization and 4-fold faster precession for the same level of polarization, leading in principle to a 16-fold gain in signal detection. In practice, relaxation effects and losses in the detector coil and sample reduce this gain; nevertheless, simulations have shown that transferring polarization from lactate $^{13}C_1$ to the methyl protons should enhance the signal by a factor of 1.9–5.4 at 3 T (Wang et al., 2017). This study also experimentally demonstrated proton detection of hyperpolarized [1-^{13}C]lactate in a tumor *in vivo* following intravenous injection of hyperpolarized [1-^{13}C]pyruvate. In effect, this experiment stores polarization in the ^{13}C nucleus, which has a relatively long polarization lifetime, before shunting the polarization onto the methyl protons for detection. Detection of substrates in which the protons have been polarized directly is more difficult *in vivo* because of their short T_1s and therefore short polarization lifetimes.

In the longer term it may be desirable to dispense with polarizer devices at each clinical site and polarize substrates at a central facility, transporting the polarized material to individual clinical sites at moderate magnetic fields and very low temperatures (at which the T_1 can be many hours). This is the model that is widely used for PET studies with the glucose analog FDG. Such a system could reduce costs and ensure a greater level of standardization. However, for this to work, the paramagnetic radical must first be separated from the polarized substrate prior to storage since the radical will relax the polarization at low magnetic fields. This can be achieved by physically separating the radical and substrate during the polarization process (Ji et al., 2017) or by creating a photo-induced radical that is stable at 1.2 K but is destroyed at higher temperatures that are below the melting point of the frozen polarized material (Capozzi et al., 2017).

Apart from brute force hyperpolarization, ^{13}C-labeled molecules can also be hyperpolarized using parahydrogen-induced polarization (Duckett and Mewis, 2012). In this experiment, spin order in parahydrogen is transferred to the molecule of interest by chemical reaction and then the proton polarization is transferred to ^{13}C at a low magnetic field. This technique has the advantage that polarization is fast and the equipment needed is relatively inexpensive, but the limitations imposed by the chemistry mean that, with the exception of succinate, none of the widely used substrates can be polarized using this technique. However, the recent development of “side arm” technology, in which carboxylic acids have been modified with a hydrogenable moiety that is cleaved following polarization transfer, means that this technique can now be used with substrates such as pyruvate and acetate (Reineri et al., 2015). The main limitation will be the level of polarization that can be achieved, which is currently much less than can be obtained by DNP. Translation of this technique to the clinic will also require efficient removal of the toxic catalyst required in the process.

Applications

Monitoring Disease Progression and Response to Treatment

Hyperpolarized [1-^{13}C]pyruvate has been the most widely used substrate because the neat acid has a high concentration and is self-glassing, the T_1 is relatively lon *in vivo*, and uptake by the monocarboxylate transporters (MCTs) and subsequent exchange of hyperpolarized ^{13}C label with the endogenous lactate pool in the reaction catalyzed by lactate dehydrogenase (LDH) is very fast. This substrate has proved to b particularly useful in tumors because they typically express high levels of the MCTs and LDH and because they frequently have high levels of lactate due to the Warburg effect (Vander Heiden and DeBerardinis, 2017). High concentrations of lactate ar

accompanied by increased NADH concentrations, and it is the NADH concentration that limits the lactate-pyruvate exchange catalyzed by LDH (Witney et al., 2011). In this specific case, however, limited polarization lifetime may be an advantage. A recer study showed that, in tumor-bearing mice, following injection of hyperpolarized [1-^{13}C]pyruvate, there were high levels of labeled lactate in the blood, which was assumed to come from other tissues, including the blood pool. However, this labeled lactate ha lost most of its polarization and therefore “wash-in” of this material into the tumor did not compromise the measurements of tumor pyruvate-lactate exchange (Serrao et al., 2018). The first-order rate constant describing this exchange is typically calculated b fitting the pyruvate and lactate signal intensities to a two-site exchange model (Day et al., 2007) or, more simply, by taking the ratio of the area under the lactate and pyruvate labeling curves (Hill et al., 2013). However, without an estimate of the pyruvat concentration reaching the tissue, the metabolically relevant flux, expressed for example in millimolar per second, cannot be calculated. A recent study using ^{14}C- and ^{13}C-labeled pyruvate showed that only ~1%–2% of the labeled pyruvate reached the tumc site, but from this concentration a metabolic flux could be calculated using the hyperpolarized ^{13}C label exchange data obtained *in vivo*. This calculated flux showed good agreement with a flux determined directly from measurements of ^{13}C-labeled lactate i tumor extracts (Serrao et al., 2016 (Please change this reference to "Serrao et al., 2018")).

Hyperpolarized [1-^{13}C]pyruvate has been used to monitor disease progression; for example, in mouse models of prostate (Albers et al., 2008) and pancreatic cancer (Serrao et al., 2016). In the first clinical study in prostate cancer, this method detected occult disease that was not visible in conventional magnetic resonance images (Nelson et al., 2013). The introduction of modern targeted therapies into the clinic has shown that patients can vary widely in their responses to treatment (Dienstmann et al., 2013). A particularly powerful application for imaging with hyperpolarized [1-^{13}C]pyruvate is in the early detection of tumor treatment response (Day et al., 2007), where it could be used to guide treatment in individual patients (Brindle, 2008). In general, response is evident as a decrease in the exchange; for example, in glioblastoma models treated with PI3K or mTOR inhibitors (Chaumeil et al., 2012; Di Gialleonardo et al., 2017; Ward et al., 2010). In a prostate cancer model treated with imatinib (Dafni et al., 2010), an inhibitor of the PDGF receptor, the exchange was decreased as a result of decreased LDHA expression. In BRAF-mutant melanoma cells, the BRAF inhibitor vemurafenib inhibited the exchange by decreasing MCT1 expression (Delgado-Goni et al., 2016). Response to radiotherapy can also be detected through a decrease in lactate-pyruvate exchange (Day et al., 2010; Saito et al., 2015). Early studies with anti-vascular agents (Bohndiek et al., 2010) and anti-angiogenic agents (Bohndiek et al., 2012) showed a decrease in the exchange, which could be explained by decreased perfusion and pyruvate delivery to the tissue. Pyruvate can also be oxidized by mitochondrial pyruvate dehydrogenase (PDH) to produce carbon dioxide, which rapidly equilibrates the hyperpolarized ^{13}C label with bicarbonate, in the reaction catalyzed by carbonic anhydrase (Gallagher et al., 2008). A subsequent study with an anti-vascular agent in a different tumor type showed no change in lactate-pyruvate exchange but an increase in the hyperpolarized [1-^{13}C]lactate/H$^{13}CO_3^-$ ratio, which was attributed to reduced respiratory activity caused by tumor hypoxia (Iversen et al., 2017). In contrast, in an orthotopic glioblastoma model treated with anti-VEGF antibody, there was an acute decrease in the hyperpolarized [1-^{13}C]lactate/H$^{13}CO_3^-$ ratio within 3 hr of drug treatment, which was attributed to a shift toward oxidative metabolism (Park et al., 2016). Disentangling the effects of perfusion from subsequent pyruvate transport and metabolism can be achieved by co-injecting a perfusion marker, such as ^{13}C-urea. In a genetically engineered mouse model of prostate cancer, higher grade tumors showed decreased perfusion associated with increased tumor hypoxia and HIF1α and VEGF expression, but increased lactate-pyruvate exchange due to upregulated expression of MCT1, MCT4, and LDHA (Chen et al., 2017). A study using another hyperpolarized ^{13}C-labeled perfusion marker (HP001) and hyperpolarized [1-^{13}C]pyruvate (Lau et al., 2016) showed a correspondence between the HP001 and lactate signals, indicating that the tumors were metabolically similar, differing only in their degree of perfusion. In this perfusion-limited case, where lactate-pyruvate exchange is fast relative to pyruvate delivery, the lactate signal could be used to assess perfusion.

Lactate labeling following hyperpolarized [1-^{13}C]pyruvate infusion can indicate whether a drug has hit its target but this does not necessarily indicate outcome. A better indicator might be tumor cell death (Neves and Brindle, 2014), and, although decreased lactate labeling can indicate cell death, it is not, as the studies above have shown, a specific indicator. Effective tumor treatments often lead to the accumulation of necrotic cells, which can be detected using hyperpolarized [1,4-$^{13}C_2$]fumarate. Fumarate enters cells slowly on the timescale of the hyperpolarization and therefore there is no detectable metabolism in viable cells. However, in necrotic cells, in which there is loss of plasma membrane integrity, fumarase, an enzyme that catalyzes the reversible hydration of fumarate to malate, can either leak out of the cells or fumarate can rapidly enter the cell and gain access to the enzyme. Under these circumstances, there is rapid formation of hyperpolarized ^{13}C-labeled malate, which acts as a positive contrast agent for the presence of necrosis. Early studies showed that it could be used to provide early evidence of tumor cell death after treatment (Gallagher et al., 2009; Witney et al., 2010) and that it was more effective at detecting low levels of diffuse necrosis than diffusion-weighted ^{1}H MRI (Bohndiek et al., 2010). The technique can also be used to detect cell death in other tissues, such as kidney (Clatworthy et al., 2012) and muscle (Eldirdiri et al., 2017). In a recent study, hyperpolarized [1-^{13}C]pyruvate, [^{13}C]urea and [1,4-$^{13}C_2$]fumarate were used to assess the effects of transcatheter arterial embolization in an orthotopic rat hepatocellular carcinoma model. There was a decrease in urea and pyruvate signals, indicating decreased perfusion; increased lactate-pyruvate exchange, consistent with increased hypoxic glycolysis; and increased production of malate, which showed a good correlation with histological assessments of necrosis (Düwel et al., 2016).

Imaging the Mutational Status of Isocitrate Dehydrogenase Gain-of-function point mutations in the isocitrate dehydrogenase 1 (IDH1) and IDH2 genes, which occur frequently in low- to intermediate-grade gliomas an secondary glioblastomas, result in a single amino acid change at the active site of the enzymes, causing the production of 2-hydroxyglutarate (2-HG) instead of α-ketoglutarate (α-KG). Inhibition of α-KG-dependent dioxygenases and demethylases by 2-HG which results in epigenetic changes and altered gene expression, have led to 2-HG being termed an oncometabolite (Cairns and Mak, 2013). There have been several studies with hyperpolarized ^{13}C-labeled substrates that have sought to detect 2-HG production, either directly or through its effects on cell metabolism. Production of [1-^{13}C]2-HG from hyperpolarized [1-^{13}C]α-KG was detected in a glioma model engineered to express mutant IDH1 (Chaumeil et al., 2013). There was also decreased conversio of [1-^{13}C]α-KG to [1-^{13}C]glutamate resulting from decreased expression of several enzymes catalyzing this conversion, which was associated with 2-HG-induced promoter methylation and silencing of the genes encoding these enzymes (Chaumeil et al., 2014 Downregulation of PDH activity, mediated by a 2-HG-dependent increase in HIF1α levels and increased expression of pyruvate dehydrogenase kinase-3, was detected as a reduction in the conversion of hyperpolarized [2-^{13}C]pyruvate to [5-^{13}C]glutamat (Izquierdo-Garcia et al., 2015). Glutamine is a primary carbon source for 2-HG and hyperpolarized [1-^{13}C]glutamine has been used to detect 2-HG production *in vivo* (Salamanca-Cardona et al., 2017).

New Substrates Despite the limitations imposed by the requirements for high solubility, long polarization lifetime, and fast metabolism, an impressive array of ^{13}C-labeled molecules have been hyperpolarized and studied *in vivo* (reviewed in Keshari an

Wilson (2014)). Some recent additions to this growing list include γ-glutamyl-[1-^{13}C]glycine, which is cleaved by a cell surface enzyme, γ-glutamyl transpeptidase (GGT), to yield free [1-^{13}C]glycine (Nishihara et al., 2016). GGT is overexpressed in severa different tumor types, including those arising in tissues that do not normally express the enzyme, such as ovarian adenocarcinoma, and it therefore has the potential to act as a tumor biomarker. ^{13}C-dihydroxyacetone has been used to probe glycolysis an gluconeogenesis in perfused mouse liver (Moreno et al., 2014), which led to labeling of glucose, glycerol 3-phosphate, phosphoenolpyruvate, pyruvate, alanine, and lactate; [1-^{13}C]glycerate has been used to probe glycolysis in rat liver *in vivo*, which led t labeling of pyruvate and lactate (Park et al., 2017). Flux in the pentose phosphate pathway (PPP) in perfused mouse liver has been assessed using hyperpolarized δ-[1-^{13}C]gluconolactone, which resulted in the production of hyperpolarized $^{13}CO_2$ (subsequentl rapidly converted to $H^{13}CO_3^-$) in the reaction catalyzed by the PPP enzyme 6-phosphogluconate dehydrogenase (Moreno et al., 2017). Flux in this pathway had previously been assessed in a murine lymphoma model using hyperpolarized [U-^{2}H, U-^{13}C]glucose where hyperpolarized label was detected in 6-phosphogluconate and again in $H^{13}CO_3^-$ (Rodrigues et al., 2014). Flux in this pathway can also be assessed by measuring the rate of reduction of hyperpolarized [1-^{13}C]dehydroascorbic acid (the oxidized form ascorbic acid) (Bohndiek et al., 2011; Keshari et al., 2011), which is dependent, at least in part, on the rate of NADPH production in the PPP (Timm et al., 2017). Extracellular pH can be determined by injecting hyperpolarized $H^{13}CO_3^-$ (Gallagher et al., 2008) an intracellular pH by injecting hyperpolarized [1-^{13}C]pyruvate (Lau et al., 2017) and measuring the $H^{13}CO_3^-/^{13}CO_2$ ratio. In the latter case, hyperpolarized $^{13}CO_2$ is produced following mitochondrial oxidation of pyruvate in the reaction catalyzed by PDH. On drawback of this technique is that it requires full equilibration of the hyperpolarized ^{13}C label between bicarbonate and CO_2, which may take some time (Wright et al., 2018). Another drawback is that the technique requires measurement of signal intensities which is often less reliable than measuring frequencies. The ^{13}C resonance frequencies of zymonic acid, which is synthesized from pyruvate, change by up to 3.0 ppm per pH unit in the physiological pH range and have been used to measure extracellular pH in kidneys and subcutaneous tumors (Düwel et al., 2017).

Concluding Remarks

With clinical studies showing that DNP-based magnetic resonance can detect tumors (Nelson et al., 2013) and monitor treatment response in prostate cancer (Aggarwal et al., 2017), the technique now stands on the threshold of wider clinical application. The challenge now is to find those applications that provide unique information and therefore that could change clinical practice. There may be an advantage in combining PET measurements of FDG uptake, which effectively monitors substrate delivery, uptake on the glucose transporters, and phosphorylation and trapping in the reaction catalyzed by the glycolytic enzyme, hexokinase, with ^{13}C magnetic resonance measurements of pyruvate-lactate exchange in the lower part of glycolysis. Arguably pyruvate gives a better indication of the Warburg effect (i.e., the failure to oxidize glucose in the presence of oxygen) than FDG-PET; where the two have been compared directly, there was a correlation between FDG uptake and lactate labeling in some but not all cases (Gutte et al., 2015). Since pyruvate does not allow whole-body imaging, it will not replace FDG-PET; for example, in order to detect the presence of metastatic disease. It may, however, have advantages for detecting disease and treatment response in some tumors; such as brain tumors (Miloushev et al., 2018), where high levels of FDG uptake in normal brain tissue can obscure uptake in the tumor. Currently the technique is expensive, although this can be expected to decrease as it becomes more widely used, particularly if it becomes possible to centralize production of the hyperpolarized substrate and then to distribute it to clinical sites.

CEST

The possibility of exploiting the superb anatomical resolution of MRI continues to make this modality highly desirable for molecular imaging applications. Among the several possibilities, the CEST approach is an emerging MRI modality that acts through the transfer of saturated magnetization to the “bulk” water signal. In other words, a CEST molecule is a system that contains one (or more) exchanging proton pool(s) that can be selectively saturated by setting a proper radiofrequency (RF) irradiating field at their absorption frequency. The transfer of saturated magnetization causes a decrease in the signal intensity in the corresponding magnetic resonance images (Figure 4A) (Ward et al., 2000).

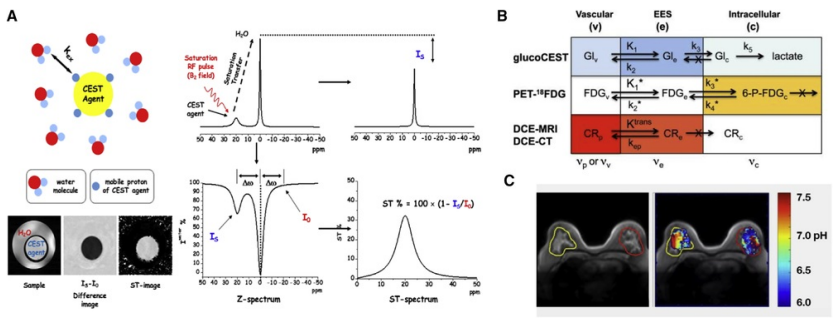

Figure 4 Imaging of Metabolism Using CEST and Gluco-CEST

(A) In CEST, RF irradiation at the absorption frequency of the mobile ^{1}H-resonance of protons in slow/intermediate exchange with water causes the transfer of saturated magnetization to the bulk water signal, which results in a decrease of signal intensity in the corresponding magnetic resonance image.

(B) Schematic showing an overview of rate constants and contrast contributions for gluco-CEST, ^{18}FDG-PET, and contrast-enhanced MRI and computed tomography (CT) in tumors. Darker color indicates higher contrast; white, negligible contrast. In gluco-CEST, glucose

concentrations in the vascular space and the EES are comparable, yet the EES contributes more to the measured signal because of its lower pH. Intracellular signal is small to negligible due to rapid glycolysis. In PET, the signal is due predominantly to trapped intracellular phosphorylated FDG. For dynamic contrast-enhanced MRI and CT, the contrast agents are found primarily in plasma and only to a small extent in EES because of the limited K^{trans}. Glucose, on the other hand, moves freely into the interstitium and the erythrocytes. v, vascular (plasma + erythrocytes); p, plasma.

(C) Image of pH heterogeneity in human breast tumor based on CEST signals from iopamidol. Provided by M. Pagel (MD Anderson Cancer Center, Houston, TX).

Principles

Being frequency-encoding systems, CEST molecules have two major advantages over the established class of relaxation enhancers: (1) more than one molecule can be detected at the same anatomical region simply by setting the RF offset of the irradiating field at the absorption frequency of the exchanging protons of the specific agents, and (2) the presence of two (or more) pools of exchanging protons on the same molecule (or single pools on molecules with analogous bio-distribution) allows the setup of ratiometric procedures for the design of responsive agents that do not require prior knowledge of the actual concentration of the contrast agent (van Zijl and Yadav, 2011). The extent of saturation transfer (ST) depends on a complex interplay among different parameters, namely the proton exchange rate, the T_1 of the water protons, and the power of the irradiating B_1 field. Comparison of ST effects obtained by applying different values of B_1 may help design alternative types of responsive procedures (Longo et al., 2014).

The disappointing major drawback of CEST-based procedures is poor sensitivity, since the concentration of exchanging protons must be in the millimolar range. In fact, the CEST effect could not be exploited if it were limited to a single transfer from the given molecule to water. The distinctive aspect of CEST is the continuous transfer of excited ^1H protons, leading to a buildup of saturation in water. Upon exchanging a saturated proton with water, that proton will be replaced with an unsaturated proton from water, which in turn can be saturated for another transfer. If this exchange takes place 100 times, then the detectability of the chemical substance (through the reduction of water signal) is well amplified. This necessary procedure makes the CEST effect dependent on the composition of the buffer solution in which the CEST molecule is dissolved. The extent of ST to the bulk water ^1H signal is dependent on chemical substance concentration, temperature, and pH. ST will continue to take place until a steady state is reached (or until the end of the RF saturation). The general rule of thumb is that the exchange process (k_{ex}) needs to be in the slow to intermediate regime on the NMR timescale. Thus $k_{ex} < \Delta\omega$, where $\Delta\omega$ is the resonance frequency difference between the exchanging proton absorption and water, in radians per second (Wu et al., 2016). In order to exploit large k_{ex} values, a class of exogenous CEST agents has been conceived based on paramagnetic complexes that display very large shifts of their proton resonances (paramagnetic CEST [para-CEST] agents) (Woessner et al., 2005). A very important feature of CEST molecules is that the contrast they induce can be switched on and off at will simply by changing the RF of irradiation. Because the contrast generated by CEST agents is frequency encoded, CEST molecules with exchangeable groups displaying different NMR chemical shifts can be simultaneously detected in the same magnetic resonance image. By assigning a given color to each contrast molecule, multicolor ^1H MRI can be obtained. This feature can be attractive for the *in vivo* detection of different CEST-active molecules co-localized in the same region, and this characteristic, although not yet fully exploited, could be particularly relevant in the field of metabolic studies.

Experimentally, the potential of a CEST agent is commonly assessed by recording its Z and ST spectra (Figure 4A). The Z spectrum reports on how the ^1H-water magnetic resonance signal intensity decreases upon changing the offset of the irradiation frequency. The signal intensity of the ^1H of water reaches zero when the offset is set at the absorption of ^1H-water resonance (direct saturation). As described above, the exchanging CEST protons decrease the water signal because of the transfer of saturated magnetization. When the chemical shift of the exchanging proton pool is close to that of bulk water, the CEST effect yields, in the Z spectrum, an asymmetry of the absorption centered at 0 ppm (bulk water is usually defined as 0 ppm in CEST experiments). In such a case, a quantitative CEST study is typically carried out by acquiring two images, one with irradiation at the CEST offset ($\Delta\omega$) and one at the opposite offset ($-\Delta\omega$). Comparison of the two images yields the percentage CEST effect (ST%), determined in the following expression as the magnetization transfer ratio (MTRasym):

$$\mathrm{MTRasym}\,(\%) = \left(1 - \frac{\mathrm{MS}\ (\Delta\omega)}{\mathrm{MS}\ (-\Delta\omega)}\right) \cdot 100 \qquad \textbf{(Equation 2)}$$

where $MS(\Delta\omega)$ and $MS(-\Delta\omega)$ are the magnetic resonance signal intensities of the bulk water protons upon applying the saturation RF field at $\Delta\omega$ and $-\Delta\omega$, respectively. The ST-spectrum reports the ST% values versus the irradiation frequency (Figure 4A).

When the endogenously occurring CEST contrast arises from amide functionalities, it is called amide proton transfer (APT). In APT imaging, endogenous mobile proteins and peptides in tissues can be detected via saturation of all the amide protons present in peptides. This imaging technique gives information about the soluble protein content, an important biomarker of many diseases, such as cancer. Other endogenous CEST reporters include glucosaminoglycans and glucose.

Endogenous CEST is analogous to magnetization transfer contrast, a contrast that is based on the irradiation of resonances of protons belonging to immobilized, semi-solid macromolecules, such as bound proteins and membranes, and to water molecules that are tightly bound to macromolecules and that are not normally visible by MRI because of their short T_2 relaxation times (bandwidth of several kilohertz) (Wolff and Balaban, 1989). Magnetization transfer contrast implies that proton saturation occurs over a large bandwidth (e.g., 50 kHz), whereas, in conventional CEST detection, the ST% effect is associated with the saturation of a specific exchanging proton resonance.

Applications

CEST Imaging of Metabolic Processes A number of endogenous substances have exchangeable protons and may therefore act as CEST imaging reporters. They include small molecules such as creatine (Cr), amino acids such as glutamat and arginine, as well as peptides and small proteins. Their CEST-MRI properties may be exploited as reporters of ongoing metabolic processes.

Creatine kinase (CK) has a crucial role in cellular energetics as it is responsible for satisfying immediate demand for ATP, which it generates from ADP and phosphocreatine (PCr):

$$PCr + ADP + H+ \rightarrow ATP + Cr \quad \textbf{(Equation 3)}$$

^{31}P-MRS has been the technique of choice for assessing CK activity and it has led to fundamental achievements in the understanding of muscle energy metabolism. Cr (Cr), PCr, and ATP, containing exchangeable protons, can be detected by CEST (Haris et al., 2012). Cr shows a faster exchange rate and often it is the species detected in CEST experiments. PCr recovery after exercise correlates well with the kinetics measured by ^{31}P-MRS. Interestingly, CrCEST can distinguish different levels of muscle use between subjects (Kogan et al., 2014). The spatial resolution and sensitivity of CrCEST are three orders of magnitude better than those of ^{31}P-MRS. CrCEST has been applied to myocardial imaging in swine and sheep with infarctions, showing that infarcted regions had lower contrast than normal myocardial regions (Haris et al., 2014). Disruption of Cr metabolism has been detected in a rat brain tumor model (Cai et al., 2015).

In tumors, the concentration of proteins may be higher than in surrounding tissues, and the increased intracellular proton exchange leads to an increased APT level. APT has been demonstrated useful to assess tumor grading; for example, it has been shown useful in predicting the histological grade of adult diffuse gliomas (Togao et al., 2014). Tumors are well known to be heterogeneous in their metabolic rates. Intra-tumor metabolic heterogeneity has been evaluated based on overall *in vivo* CEST-MRI contrast arising from metabolites such as glutamate, alanine, and Cr. A significant correlation has been reported between the CEST contrast generated by these metabolites and the tissue mitochondrial NADH and the NADH redox ratio measured by redox scanning in breast cancer (Cai et al., 2014). The CEST response from glutamate (GluCEST) has attracted much attention and continues to be a subject of intense scrutiny (Davis et al., 2015).

An interesting approach is to engineer cells to express CEST-active polypeptides that may act as imaging gene reporters to enable the monitoring of the transcriptional and translational regulation of genes. Following transfection or transduction, and upon activation of the gene promoter, the gene product can be properly detected by the CEST procedure. This approach may become very useful to monitor the efficacy of gene therapies; the survival, migration, and differentiation of transplanted stem cells; and a variety of molecular events. The method was tested to generate two types of gene products: (1) peptides and (2) enzymes. Among peptides, the most studied system is represented by poly-L-lysine, which is able to yield a high CEST contrast upon the saturation of its exchangeable amide protons. This procedure was applied in transduced 9L rat gliosarcoma cells (Gilad et al., 2007). Genetically encoded enzymes have been proposed as systems able to report on phosphorylation/dephosphorylation processes. For instance, protein kinase A (PKA) phosphorylates the OH group of serine and threonine, with high specificity for a given amino acid sequence. PKA peptide-based sequences have been screened and the resulting CEST signal assessed (Airan et al., 2012).

Among diamagnetic CEST agents, it is worth mentioning a system that quantitatively detects β-galactosidase and β-glucuronidase activities (Fernández-Cuervo et al., 2016). Using a modular approach, the authors designed the enzyme substrates to incorporate a salicylate moiety with a chromogenic spacer via a carbamate linkage. This structural motif furnishes highly selective diamagnetic CEST agents that detect and quantify activities of glycoside hydrolase enzymes. Furthermore, a variety of diamagnetic agents have been developed that detect enzyme activity *in vitro* and *in vivo*; for example, γ-glutamyl transferase (Sinharay et al., 2017) and cathepsin B (Hingorani et al., 2016). In another interesting example (Liu et al., 2011), researchers detected cytosine deaminase activity by tracking the loss of CEST signal during the transformation of 5-fluorocytosine to 5-fluorouracil.

Several para-CEST agents have been developed for the detection of enzymatic activity. These systems share a common amino acid sequence on the external surface of the paramagnetic complex. The cleavage of the sequence by the enzyme appears as changes in the CEST spectra (position of proton-exchanging groups and ST efficiency), allowing the definition of ratiometric methods that report on specific enzymatic activity. Systems designed to assess the protease activity of caspase-3 (Yoo and Pagel, 2006), cathepsin D (Suchý et al., 2010), and urokinase plasminogen activator (Yoo et al., 2014) have been reported. A para-CEST agent was also conceived to assess transglutaminase activity. Since this enzyme catalyzes the formation of a bond between a lysine and glutamine, transforming an amine into an amide group, the underlying transformation results in a marked change in the rate of prototropic exchange (fast for the amine functionality, slow for the amide functionality) (Hingorani et al., 2013).

Chemists have shown that quantitative determination of specific metabolites can be pursued through a proper design of para-CEST agents. By this approach, not yet tested *in vivo*, metabolites such lactate (Aime et al., 2002b; Zhang et al., 2017), methyl phosphate (Huang and Morrow, 2009), and glucose (Trokowski et al., 2004) have been assessed through reversible changes in the CEST properties. Moreover, irreversible changes in the structure of the para-CEST agent can also be exploited, as shown in the case of the determination of NO (Liu et al., 2007).

An important task deals with the assessment of the redox state of tissues, as many pathologies are characterized by dysregulated concentrations of reducing agents. Therefore, chemical structures of para-CEST agents have been designed to undergo reversible changes in response to the redox state (Ratnakar et al., 2012). As above, the structural changes are reflected in a modulation of the CEST properties. However, the structural changes may also have large effects on the chemical shifts of the proton-exchanging resonances, and often this effect is eventually preferred because the chemical shift is independent of the agent's concentration.

Gluco-CEST Since the discovery of the Warburg effect, cancer metabolism has been intensively studied, leading many to search for CEST-based imaging procedures for cancer detection and diagnosis. The vast majority of cancers exhibit increase glucose uptake and glycolysis regardless of oxygen availability. Glycolytic cells are considered hypermetabolic because they tend to take up much more glucose than surrounding, healthy tissue, and they tend to proliferate rapidly. The CEST response fro

administered glucose (gluco-CEST) has therefore received considerable attention. Tumors can be visualized via the detection of saturated magnetization from glucose hydroxyl groups (Chan et al., 2012). Feasibility was established in phantoms as well a *in vivo* using two human breast cancer cell lines, MDA-MB-231 and MCF-7, which were implanted orthotopically in nude mice. The obtained results were compared with PET and contrast-enhanced MRI. Both tumor types exhibited significant gluco-CES signal enhancement during systemic sugar infusion (mild hyperglycemia), allowing their non-invasive visualization. Gluco-CEST showed differences between tumor types, while PET and contrast-enhanced MRI did not. Data were discussed in terms of signa contributions from the increased vascular volume in tumors and especially from the acidic extracellular extravascular space (EES), where gluco-CEST signal is expected to be enhanced due to a slowdown of hydroxyl proton exchange (Figure 4B).

Golay and coworkers further investigated the gluco-CEST approach to detect glucose uptake in tumors, and to compare it with standard markers of tumor metabolism and pathophysiology, such as hypoxia and blood flow (Walker-Samuel et al., 2013). They performed a gluco-CEST imaging experiment (GCE), and compared the results 24 hr later with FDG autoradiography. Two subcutaneous human colorectal tumor xenograft models were evaluated, LS174T and SW1222, which had markedly different phenotypes. It was shown that median tumor GCE and FDG uptake values were significantly correlated, thereby providing a validation of the gluco-CEST technique. They concluded that the source of the gluco-CEST signal could be attributed to both intra- and extracellular compartments, which explains its agreement with FDG autoradiography measurements.

The resolution of modern PET systems (typically on the order of $5 \times 5 \times 5$ mm^3) is much lower than the resolution afforded by clinical MRI scanners (typically around $1 \times 1 \times 3$ mm^3), corresponding to a 40-fold decrease in voxel size. Gluco-CEST may offer considerable improvements in spatial resolution over FDG-PET. Such improvements would allow intra-tumor heterogeneity to be more effectively probed and would allow evaluation of smaller tumor masses, thereby permitting earlier characterization of disease and assessment of response to therapy. The gluco-CEST procedure has been tested clinically in head and neck cancer using a clinical 3-T MRI scanner (Wang et al., 2016).

A limit on the use of glucose is that one cannot distinguish between intra- and extracellular compartments. This issue has been successfully tackled by using glucose analogs that are not metabolized once they have entered the cell. Navon and coworkers evaluated the feasibility of detecting tumors and metastases by the CEST-MRI technique using 3-*O*-methyl-D-glucose (3OMG), a non-metabolizable derivative of glucose that is taken up rapidly and preferentially by tumors and is entirely excreted by the kidneys (Rivlin et al., 2014). Following intraperitoneal injection of 3OMG (1.5 g/kg), an enhanced CEST effect of approximately 20% was visualized at the tumor within a few minutes. The signal slowly declined, reaching half of its maximum at approximately 80 min.

Acido-CEST Agents As it is well established that enhanced glycolysis results in a more acidic EES, the CEST mapping of pH in EES has been the subject of a number of investigations (Gillies and Gatenby, 2007). These studies were performed by usin pH reporters able to act without prior knowledge of their *in vivo* concentrations. Both diamagnetic and paramagnetic CEST systems were investigated for this application. The preferred agents are represented by systems containing two sets of exchangin protons as the ratio of the relative ST effects versus pH, allowing the determination of pH measurements that are independent of the actual concentration of the agent. Para-CEST agents have the advantage of displaying larger chemical shifts of th exchanging proton resonances, thus allowing the exploitation of larger k_{ex} values. Despite the promise of acido-CEST, application of this technique may be hampered by the difficulty in delivering sufficient concentrations of agents *in vivo*.

The first reported acido-CEST agents were a series of lanthanide(III) complexes of Eu, Dy, Ho, Er, Tm, or Yb with the macrocyclic DOTAM-Gly ligand, which is the tetraglycine amide derivative of 1,4,7,10-tetraazacyclododecane-1,4,7,10-tetraacetic acid (DOTA) (Aime et al., 2002a). These complexes possess two pools of exchangeable protons: the coordinated water and amide protons. Yb-DOTAM-Gly displays the most interesting CEST properties when its amide N-H resonance (16 ppm upfield H_2O signal) is irradiated. As the exchange rate of amide protons is base-catalyzed, Yb-DOTAM-Gly turns out to be an efficient pH-responsive probe in the pH range of 5.5–8.1. A ratiometric method has been set up by the use of a mixture of Eu-DOTAM-Gly and Yb-DOTAM-Gly, whose exchangeable proton pools are, respectively, the coordinated water (~40 ppm downfield H_2O signal at 312 K) and the amide protons. This approach yields a pH-dependent CEST effect that is a function of the concentration ratio of the two complexes.

Yb-HPDO3A, an analog of a clinically approved Gd agent, was tested for *in vivo* pH mapping of the tumor region in a melanoma murine model (Delli Castelli et al., 2014). CEST magnetic resonance images of tumor and bladder were acquired after intravenous administration of Yb-HPDO3A (1.2 mmol/kg). Yb-HPDO3A distributes well in the extracellular space of the tumor, allowing the detection of good levels of ST. It is excreted throughout kidneys and accumulated in the bladder, thus yielding a strong CEST signal from urine. By comparing the ST% obtained upon selective irradiation of the two OH resonances belonging to the two isomeric forms of Yb-HPDO3A, it is possible to measure the extracellular pH for each voxel (0.22 mm^3). The obtained pH maps of tumors show great heterogeneity. Marked differences are associated with tumor staging.

Another para-CEST agent for pH mapping is Yb-DO3A-oAA, which can be used *in vivo* only in combination with a rapid CEST-MRI protocol called CEST-FISP MRI (Sheth et al., 2012). In addition, much work has been done to use X-ray contrast agents as CEST-MRI reporters. The structures of these highly hydrophilic molecules contain exchangeable protons (e.g., amide and alcoholic protons) that can be exploited for the generation of the CEST effect. Iopamidol (Isovue, Bracco Diagnostics) has been extensively investigated as it contains two types of amide functionalities, for which the exchange rate of the two amide proton pools is markedly pH dependent. Thus, a ratiometric method for pH assessment has been set up based on the comparison of the ST effects induced by selective irradiation of the two resonances. This ratiometric approach means that the concentration effect of the contrast agent can be excluded, and it provides accurate pH measurements in the range of 5.5–7.4 (Longo et al., 2011). This approach has recently been extended to cancer patients, providing excellent representation of pH heterogeneity in the tumor region (Jones et al., 2017) (Figure 4C).

The observation of B_1-dependent CEST measurement enables a novel ratiometric calculation by comparing ST effects obtained at two or more RF irradiation powers from a single labile proton group. On this basis, a new ratiometric index, dubbed ratio of RF power mismatch (RPM), can be determined according to:

$$\mathrm{RPM}=\frac{\left[(1-\mathrm{ST})/\mathrm{ST}\right]_{\mathrm{RF1}}}{\left[(1-\mathrm{ST})/\mathrm{ST}\right]_{\mathrm{RF2}}} \quad \textbf{(Equation 4)}$$

where $\mathrm{ST}_{\mathrm{RF1,2}}$ represents ST obtained at different RF power levels. The proposed RPM was calculated as a function of pH. When used to calculate the ratio of ST effects between RF power levels of 3 and 6 μT, RPM showed a good pH response at pHs from 6.0 to 7.4. The molecule of choice for the application of this approach was iobitridol, an X-ray contrast agent analog of iopamidol with only a single set of amide protons (Longo et al., 2014).

CEST-MRI pH mapping allows the monitoring of changes in tumor acidosis to assess treatment response to dichloroacetate, a drug that can reverse the glycolytic phenotype that is responsible for increased lactate production and extracellular pH acidification in cancer cells. Dichloroacetate acts by inhibiting pyruvate dehydrogenase kinase. Tumor-bearing mice showed a marked and significant increase in tumor extracellular pH at 3 days after dichloroacetate treatment, reflecting dichloroacetate-induced glycolysis inhibition, as confirmed by reduced lactate production (Anemone et al., 2017).

The *in vivo* correlation between tumor FDG uptake and extracellular pH values in a murine model of $\mathrm{HER2}^{+}$ breast cancer has been assessed using iopamidol as the CEST-MRI agent. The combination of PET and CEST-MRI images reported complementary spatial information of the altered glucose metabolism. Notably, a significant inverse correlation was found between extracellular tumor pH and FDG uptake: high FDG uptake was associated with lower extracellular pH. These results definitively show how merging the information from FDG uptake and extracellular pH measurements can improve characterization of the tumor microenvironment (Longo et al., 2016).

Concluding Statements

The metabolic information that can be obtained *in vivo* from several endogenous CEST-responsive metabolites may greatly enhance our understanding of the underlying processes. In general, CEST allows access to information that, to some extent, is analogous to the information attainable from MRS and MRS imaging, with the advantage that the use of the intense water signal provides images with higher spatial resolution from voxels of markedly smaller size. Of course, CEST is limited to metabolites containing exchangeable protons or to the assessment of substrates (e.g., enzymes) that can be detected by exogenous CEST agents. The method appears particularly valuable in the characterization of whole-tumor metabolism, as it may meet additional challenges in accurately imaging tumor metabolic heterogeneity. Moreover, exogenous CEST agents as well as properly engineered gene reporters may be designed to widen the number of (patho)physiological processes that can be tackled with this technique. The sensitivity of CEST procedures may not yet be high enough to provide a complete picture of tumor metabolism, but continuous improvements in the hardware and image processing make us confident that the CEST approach will occupy a central place in the armory of imaging tools to more finely study *in vivo* metabolic processes.

Summary

Studies of metabolism benefit from the ability to observe living systems and dynamic processes. Therefore, imaging is a critical tool in understanding metabolic processes from the cellular to the system level. In this review, we have focused on methods that do not use ionizing radiation and therefore are in principle appropriate for longitudinal dynamic studies. Nevertheless, all methods presented come with strengths and limitations and attain different operational characteristics, in particular with respect to scale; i.e., the field of view and the depth of visualization.

Optical microscopy has always played a major role in biomedical discovery. Initial auto-fluorescence studies of tissue metabolites are now complemented with powerful novel techniques such as Raman and mid-infrared sensing and allow label-free imaging of an extended number of metabolites. While optical microscopy is limited to superficial depths of a few tens to hundreds of micrometers, optoacoustic methods yield new capabilities to generate high-resolution quantitative images of hemoglobins and lipids to depths of several millimeters to centimeters in tissue. Optoacoustic methods can use spectral technology to unmix the contributions of these tissue compartments. However, currently the technique is limited to indirect observations of metabolic processes, in particular through visualizing oxygen utilization and TBV changes due to increased metabolic demand. In this way, novel ultrasonography methods could also reveal perfusion changes associated with metabolic demand; however, the ability of optoacoustics to resolve oxygenated and deoxygenated hemoglobin and infer oxygen utilization is perhaps more relevant for aerobic metabolism studies. Optoacoustics leads to portable implementations and can combine ultrasound and optical contrast in one modality. Therefore, it may lead to novel applications of point-of-care measurements of metabolic profiles that were never possible before. The use of contrast agents can increase the application profile of these methods. However, similarly to ultrasonography, optoacoustic imaging will be limited to superficial imaging and niche applications associated with superficial signals, such as brown fat, subcutaneous lipid metabolism, or muscle energetics.

Conversely, non-ionizing imaging deeper in tissue and whole-body interrogations can rely on magnetic resonance techniques. While MRS can resolve metabolites with great specificity, hyperpolarized MRI and CEST-MRI are emerging as methods with the potential to improve detection sensitivity and play an increasingly important role in the study of metabolic processes and the detection of disease based on disturbed metabolic profiles. With increasing demand to assess metabolic processes *in vivo*, imaging is similarly expected to play an increasingly central role in research and clinical applications, enhancing not only the depth of investigations by improving the contrast and amount of information visualized but also the breadth of possible studies by allowing new portable and non-ionizing ways to dynamically observe tissues.

Acknowledgments

We acknowledge useful discussions with Angelos Karlas, MD, and support to V.N. from the European Research Council within the European Union's Horizon 2020 research and innovation program under grant agreement 694968 (PREMSOT) and from the Deutsche Forschungsgemeinschaft (Gottfried Wilhelm Leibniz Prize 2013; NT 3/10-1). The work in K.M.B.'s laboratory is supported by Cancer Research UK (grants A/17242, A/16465, A/25040).

Declaration of Interests

V.N. holds equity in iThera Medical, serves as a consultant to SurgVision, and holds patents related to several aspects of optoacoustic technology, including MSOT. S.A. has research agreements with Bracco Imaging, with which he holds patents on MRI-pH mapping with CEST agents. K.M.B. has research agreements with GE Healthcare, with which he holds patents on some aspects of hyperpolarized ^{13}C technology.

References

Aggarwal R., Vigneron D.B. and Kurhanewicz J., Hyperpolarized [1-^{13}C]-pyruvate magnetic resonance imaging detects an early metabolic response to androgen ablation therapy in prostate cancer, *Eur. Urol.* **72**, 2017, 1028–1029.

Aguirre J., Schwarz M., Garzorz N., Omar M., Buehler A., Eyerich K. and Ntziachristos V., Precision assessment of label-free psoriasis biomarkers with ultra-broadband optoacoustic mesoscopy, *Nat. Biomed. Eng.* **1**, 2017, 0068.

Aime S., Barge A., Delli Castelli D., Fedeli F., Mortillaro A., Nielsen F.U. and Terreno E., Paramagnetic lanthanide(III) complexes as pH-sensitive chemical exchange saturation transfer (CEST) contrast agents for MRI applications, *Magn. Reson. Med.* **47**, 2002a, 639–648.

Aime S., Delli Castelli D., Fedeli F. and Terreno E., A paramagnetic MRI-CEST agent responsive to lactate concentration, *J. Am. Chem. Soc.* **124**, 2002b, 9364–9365.

Airan R.D., Bar-Shir A., Liu G., Pelled G., McMahon M.T., van Zijl P.C., Bulte J.W. and Gilad A.A., MRI biosensor for protein kinase A encoded by a single synthetic gene, *Magn. Reson. Med.* **68**, 2012, 1919–1923.

Albers M.J., Bok R., Chen A.P., Cunningham C.H., Zierhut M.L., Zhang V.Y., Kohler S.J., Tropp J., Hurd R.E., Yen Y.F., et al., Hyperpolarized ^{13}C lactate, pyruvate, and alanine: noninvasive biomarkers for prostate cancer detection and grading, *Cancer Res.* **68**, 2008, 8607–8615.

Ale A., Ermolayev V., Herzog E., Cohrs C., de Angelis M.H. and Ntziachristos V., FMT-XCT: in vivo animal studies with hybrid fluorescence molecular tomography-X-ray computed tomography, *Nat. Methods* **9**, 2012, 615–620.

Anemone A., Consolino L., Conti L., Reineri F., Cavallo F., Aime S. and Longo D.L., In vivo evaluation of tumour acidosis for assessing the early metabolic response and onset of resistance to dichloroacetate by using magnetic resonance pH imaging, *Int. J. Oncol.* **51**, 2017, 498–506.

Ardenkjaer-Larsen J.H., Fridlund B., Gram A., Hansson G., Hansson L., Lerche M.H., Servin R., Thaning M. and Golman K., Increase in signal-to-noise ratio of > 10,000 times in liquid-state NMR, *Proc. Natl. Acad. Sci. USA* **100**, 2003, 10158–10163.

Avison M.J., Hetherington H.P. and Shulman R.G., Applications of NMR studies to tissue metabolism, *Ann. Rev. Biophys. Chem.* **15**, 1986, 377–402.

Bai Y., Zhang D., Li C., Liu C. and Cheng J.-X., Bond-selective imaging of cells by mid-infrared photothermal microscopy in high wavenumber region, *J. Phys. Chem. B* **121**, 2017, 10249–10255.

Baker M.J., Trevisan J., Bassan P., Bhargava R., Butler H.J., Dorling K.M., Fielden P.R., Fogarty S.W., Fullwood N.J., Heys K.A., et al., Using Fourier transform IR spectroscopy to analyze biological materials, *Nat. Protoc.* **9**, 2014, 1771–1791.

Bauwens M., Wierts R., van Royen B., Bucerius J., Backes W., Mottaghy F. and Brans B., Molecular imaging of brown adipose tissue in health and disease, *Eur. J. Nucl. Med. Mol. Imaging* **41**, 2014, 776–791.

Boezeman R.P., Moll F.L., Ünlü Ç. and de Vries J.P., Systematic review of clinical applications of monitoring muscle tissue oxygenation with near-infrared spectroscopy in vascular disease, *Microvasc. Res.* **104**, 2016, 11–22.

Bohndiek S.E., Kettunen M.I., Hu D.-E. and Brindle K.M., Hyperpolarized ^{13}C spectroscopy detects early changes in tumor vasculature and metabolism after VEGF neutralization, *Cancer Res.* **72**, 2012, 854–864.

Bohndiek S.E., Kettunen M.I., Hu D.-E., Kennedy B.W.C., Boren J., Gallagher F.A. and Brindle K.M., Hyperpolarized [1-^{13}C]-ascorbic and dehydroascorbic acid: vitamin C as a probe for imaging redox status in vivo, *J. Am. Chem. Soc.* **133**, 2011, 11795–11801.

Bohndiek S.E., Kettunen M.I., Hu D.E., Witney T.H., Kennedy B.W.C., Gallagher F.A. and Brindle K.M., Detection of tumor response to a vascular disrupting agent by hyperpolarized ^{13}C magnetic resonance spectroscopy, *Mol. Cancer Ther.* **9**, 2010, 3278–3288.

Bornet A., Melzi R., Perez Linde A.J., Hautle P., van den Brandt B., Jannin S. and Bodenhausen G., Boosting dissolution dynamic nuclear polarization by cross polarization, *J. Phys. Chem. Lett.* **4**, 2013, 111–114.

Brindle K., New approaches for imaging tumour responses to treatment, *Nat. Rev. Cancer* **8**, 2008, 94–107.

Brindle K.M., Imaging metabolism with hyperpolarized ^{13}C-labeled cell substrates, *J. Am. Chem. Soc.* **137**, 2015, 6418–6427.

Brindle K.M., Boyd J., Campbell I.D., Porteous R. and Soffe N., Observation of carbon labelling in cell metabolites using proton spin echo NMR, *Biochem. Biophys. Res. Commun.* **109**, 1982a, 864–871.

Brindle K.M., Brown F.F., Campbell I.D., Foxall D.L. and Simpson R.J., A ^{1}H n.m.r. study of isotope exchange catalyzed by glycolytic-enzymes in the human-erythrocyte, *Biochem. J.* **202**, 1982b, 589–602.

Brindle K.M. and Campbell I.D., ^{1}Hydrogen nuclear magnetic resonance studies of cells and tissues, In: James T.L. and Margulis A.R., (Eds.), *Biomedical Magnetic Resonance,* 1984, Radiology Research and Education Foundation, 243–255.

Cai K., Singh A., Poptani H., Li W., Yang S., Lu Y., Hariharan H., Zhou X.J. and Reddy R., CEST signal at 2 ppm (CEST@2ppm) from Z-spectral fitting correlates with creatine distribution in brain tumor, *NMR Biomed.* **28**, 2015 1–8.

Cai K., Xu H.N., Singh A., Moon L., Haris M., Reddy R. and Li L.Z., Breast cancer redox heterogeneity detectable with chemical exchange saturation transfer (CEST) MRI, *Mol. Imaging Biol.* **16**, 2014, 670–679.

Cairns R.A. and Mak T.W., Oncogenic isocitrate dehydrogenase mutations: mechanisms, models, and clinical opportunities, *Cancer Discov.* **3**, 2013, 730–741.

Capozzi A., Cheng T., Boero G., Roussel C. and Comment A., Thermal annihilation of photo-induced radicals following dynamic nuclear polarization to produce transportable frozen hyperpolarized 13C-substrates, *Nat. Commun.* **8**, 2017, 15757.

Chan K.W., McMahon M.T., Kato Y., Liu G., Bulte J.W., Bhujwalla Z.M., Artemov D. and van Zijl P.C., Natural D-glucose as a biodegradable MRI contrast agent for detecting cancer, *Magn. Reson. Med.* **68**, 2012, 1764–1773.

Chatni M.R., Xia J., Sohn R., Maslov K., Guo Z., Zhang Y., Wang K., Xia Y., Anastasio M., Arbeit J., et al., Tumor glucose metabolism imaged in vivo in small animals with whole-body photoacoustic computed tomography, *J. Biomed. Opt.* **17**, 2012, 076012.

Chaumeil M.M., Larson P.E., Woods S.M., Cai L., Eriksson P., Robinson A.E., Lupo J.M., Vigneron D.B., Nelson S.J., Pieper R.O., et al., Hyperpolarized [1-^{13}C] glutamate: a metabolic imaging biomarker of IDH1 mutational status in glioma, *Cancer Res.* **74**, 2014, 4247–4257.

Chaumeil M.M., Larson P.E., Yoshihara H.A., Danforth O.M., Vigneron D.B., Nelson S.J., Pieper R.O., Phillips J.J. and Ronen S.M., Non-invasive in vivo assessment of IDH1 mutational status in glioma, *Nat. Commun.* **4**, 2013, 2429.

Chaumeil M.M., Ozawa T., Park I., Scott K., James C.D., Nelson S.J. and Ronen S.M., Hyperpolarized ^{13}C MR spectroscopic imaging can be used to monitor Everolimus treatment in vivo in an orthotopic rodent model of glioblastoma, *Neuroimage* **59**, 2012, 193–201.

Chen H.Y., Larson P.E.Z., Bok R.A., von Morze C., Sriram R., Delos Santos R., Delos Santos J., Gordon J.W., Bahrami N., Ferrone M., et al., Assessing prostate cancer aggressiveness with hyperpolarized dual-agent 3D dynamic imaging of metabolism and perfusion, *Cancer Res.* **77**, 2017, 3207–3216.

Cheng J.X. and Xie X.S., Vibrational spectroscopic imaging of living systems: an emerging platform for biology and medicine, *Science* **350**, 2015, aaa8870.

Cheng T., Mishkovsky M., Bastiaansen J.A., Ouari O., Hautle P., Tordo P., van den Brandt B. and Comment A., Automated transfer and injection of hyperpolarized molecules with polarization measurement prior to in vivo NMR, *NMR Biomed.* **26**, 2013, 1582–1588.

Clatworthy M.R., Kettunen M.I., Hu D.E., Mathews R.J., Witney T.H., Kennedy B.W.C., Bohndiek S.E., Gallagher F.A., Jarvis L.B., Smith K.G.C., et al., Magnetic resonance imaging with hyperpolarized [1,4-$^{13}C_2$] fumarate allows detection of early renal acute tubular necrosis, *Proc. Natl. Acad. Sci. USA* **109**, 2012, 13374–13379.

Cohen S.M., Shulman R.G. and McLaughlin A.C., Effects of ethanol on alanine metabolism in perfused mouse liver studied by 13C NMR, *Proc. Natl. Acad. Sci. USA* **76**, 1979, 4808–4812.

Comment A. and Merritt M.E., Hyperpolarized magnetic resonance as a sensitive detector of metabolic function, *Biochemistry* **53**, 2014, 7333–7357.

Cunningham C.H., Lau J.Y., Chen A.P., Geraghty B.J., Perks W.J., Roifman I., Wright G.A. and Connelly K.A., Hyperpolarized ^{13}C metabolic MRI of the human heart: initial experience, *Circ. Res.* **119**, 2016, 1177–1182.

Dafni H., Larson P.E., Hu S., Yoshihara H.A., Ward C.S., Venkatesh H.S., Wang C., Zhang X., Vigneron D.B. and Ronen S.M., Hyperpolarized ^{13}C spectroscopic imaging informs on hypoxia-inducible factor-1 and myc activity downstream of platelet-derived growth factor receptor, *Cancer Res.* **70**, 2010, 7400–7410.

Davis K.A., Nanga R.P., Das S., Chen S.H., Hadar P.N., Pollard J.R., Lucas T.H., Shinohara R.T., Litt B., Hariharan H., et al., Glutamate imaging (GluCEST) lateralizes epileptic foci in nonlesional temporal lobe epilepsy, *Sci. Transl. Med.* **7**, 2015, 309ra161.

Day S.E., Kettunen M.I., Cherukuri M.K., Mitchell J.B., Lizak M.J., Morris H.D., Matsumoto S., Koretsky A.P. and Brindle K.M., Detecting response of rat C6 glioma tumors to radiotherapy using hyperpolarized [1-^{13}C]pyruvate and ^{13}C magnetic resonance spectroscopic imaging, *Magn. Reson. Med.* **65**, 2010, 557–563.

Day S.E., Kettunen M.I., Gallagher F.A., Hu D.E., Lerche M., Wolber J., Golman K., Ardenkjaer-Larsen J.H. and Brindle K.M., Detecting tumor response to treatment using hyperpolarized ^{13}C magnetic resonance imaging and spectroscopy, *Nat. Med.* **13**, 2007, 1382–1387.

Deán-Ben X.L., Fehm T.F., Ford S.J., Gottschalk S. and Razansky D., Spiral volumetric optoacoustic tomography visualizes multi-scale dynamics in mice, *Light Sci. Appl.* **6**, 2017a, e16247.

Deán-Ben X.L., Gottschalk S., McLarney B., Shoham S. and Razansky D., Advanced optoacoustic methods for multiscale imaging of in vivo dynamics, *Chem. Soc. Rev.* **46**, 2017b, 2158–2198.

DeGrado T.R., Bhattacharyya F., Pandey M.K., Belanger A.P. and Wang S., Synthesis and preliminary evaluation of 18-(18)F-fluoro-4-thia-oleate as a PET probe of fatty acid oxidation, *J. Nucl. Med.* **51**, 2010, 1310–1317.

Delgado-Goni T., Miniotis M.F., Wantuch S., Parkes H.G., Marais R., Workman P., Leach M.O. and Beloueche-Babari M., The BRAF inhibitor vemurafenib activates mitochondrial metabolism and inhibits hyperpolarized pyruvate-lactate exchange in BRAF-mutant human melanoma cells, *Mol. Cancer Ther.* **15**, 2016, 2987–2999.

Delli Castelli D., Ferrauto G., Cutrin J.C., Terreno E. and Aime S., In vivo maps of extracellular pH in murine melanoma by CEST-MRI, *Magn. Reson. Med.* **71**, 2014, 326–332.

Di Gialleonardo V., Aldeborgh H.N., Miloushev V., Folkers K.M., Granlund K., Tap W.D., Lewis J.S., Weber W.A. and Keshari K.R., Multinuclear NMR and MRI reveal an early metabolic response to mTOR inhibition in sarcoma, *Cancer Res.* **77**, 2017, 3113–3120.

Dienstmann R., Rodon J., Barretina J. and Tabernero J., Genomic medicine frontier in human solid tumors: prospects and challenges, *J. Clin. Oncol.* **31**, 2013, 1874–1884.

Dima A., Burton N.C. and Ntziachristos V., Multispectral optoacoustic tomography (MSOT) at 64, 128 and 256 channels, *J. Biomed. Opt.* **19**, 2014, 36021.

Diot G., Dima A. and Ntziachristos V., Multispectral opto-acoustic tomography of exercised muscle oxygenation, *Opt. Lett.* **40**, 2015, 1496.

Diot G., Metz S., Noske A., Liapis E., Schroeder B., Ovsepian S.V., Meier R., Rummeny E.J. and Ntziachristos V., Multi-spectral optoacoustic tomography (MSOT) of human breast cancer, *Clin. Cancer Res.* **23**, 2017, 6912.

Duckett S.B. and Mewis R.E., Application of parahydrogen induced polarization techniques in NMR spectroscopy and imaging, *Acc. Chem. Res.* **45**, 2012, 1247–1257.

Düwel S., Durst M., Gringeri C.V., Kosanke Y., Gross C., Janich M.A., Haase A., Glaser S.J., Schwaiger M., Schulte R.F., et al., Multiparametric human hepatocellular carcinoma characterization and therapy response evaluation by hyperpolarized ^{13}C MRSI, *NMR Biomed.* **29**, 2016, 952–960.

Düwel S., Hundshammer C., Gersch M., Feuerecker B., Steiger K., Buck A., Walch A., Haase A., Glaser S.J., Schwaiger M., et al., Imaging of pH in vivo using hyperpolarized ^{13}C-labelled zymonic acid, *Nat. Commun.* **8**, 2017, 15126.

Eldirdiri A., Clemmensen A., Bowen S., Kjær A. and Ardenkjær-Larsen J.H., Simultaneous imaging of hyperpolarized [1,4-$^{13}C_2$]fumarate, [1-^{13}C]pyruvate and ^{18}F–FDG in a rat model of necrosis in a clinical PET/MR scanner, *NMR Biomed.* **30**, 2017, e3803.

Fernández-Cuervo G., Tucker K.A., Malm S.W., Jones K.M. and Pagel M.D., Diamagnetic imaging agents with a modular chemical design for quantitative detection of β-galactosidase and β-glucuronidase activities with catalyCEST MRI, *Bioconjug. Chem.* **27**, 2016, 2549–2557.

Gadian D.G. and Radda G.K., NMR studies of tissue metabolism, *Ann. Rev. Biochem.* **50**, 1981, 69–83.

Gallagher F., Kettunen M., Day S., Hu D.-E., Ardenkjaer-Larsen J.H., Zandt R.I., Jensen P.R., Karlsson M., Golman K., Lerche M.H., et al., Magnetic resonance imaging of pH *in vivo* using hyperpolarized ^{13}C-labeled bicarbonate, *Nature* **453**, 2008, 940–943.

Gallagher F.A., Kettunen M.I., Hu D.E., Jensen P.R., Zandt R.I., Karlsson M., Gisselsson A., Nelson S.K., Witney T.H., Bohndiek S.E., et al., Production of hyperpolarized [1,4-$^{13}C_2$]malate from [1,4-$^{13}C_2$]fumarate is a marker of cell necrosis and treatment response in tumors, *Proc. Natl. Acad. Sci. USA* **106**, 2009, 19801–19806.

Geltman E.M., Assessment of myocardial fatty acid metabolism with 1-11C-palmitate, *J. Nucl. Cardiol.* **1**, 1994, S15–S22.

Geraghty B.J., Lau J.Y., Chen A.P. and Cunningham C.H., Accelerated 3D echo-planar imaging with compressed sensing for time-resolved hyperpolarized (13) C studies, *Magn. Reson. Med.* **77**, 2017, 538–546.

Ghazaryan A., Ovsepian S.V. and Ntziachristos V., Extended near-infrared optoacoustic spectrometry for sensing physiological concentrations of glucose, *Front. Endocrinol. (Lausanne)* **9**, 2018, 112.

Gilad A.A., McMahon M.T., Walczak P., Winnard P.T., Jr., Raman V., van Laarhoven H.W., Skoglund C.M., Bulte J.W. and van Zijl P.C., Artificial reporter gene providing MRI contrast based on proton exchange, *Nat. Biotechnol.* **25**, 2007, 217–219.

Gillies R.J. and Gatenby R.A., Adaptive landscapes and emergent phenotypes: why do cancers have high glycolysis?, *J. Bioenerg. Biomembr.* **39**, 2007, 251–257.

Golman K., Zandt R.I., Lerche M., Pehrson R. and Ardenkjaer-Larsen J.H., Metabolic imaging by hyperpolarized ^{13}C magnetic resonance imaging for in vivo tumor diagnosis, *Cancer Res.* **66**, 2006, 10855–10860.

Grassi I., Nanni C., Allegri V., Morigi J.J., Montini G.C., Castellucci P. and Fanti S., The clinical use of PET with 11C-acetate, *Am. J. Nucl. Med. Mol. Imaging* **2**, 2012, 33–47.

Gropler R.J., Radionuclide imaging of myocardial metabolism, *Circ. Cardiovasc. Imaging* **3**, 2010, 211–222.

Gutte H., Hansen A.E., Larsen M.M., Rahbek S., Henriksen S.T., Johannesen H.H., Ardenkjaer-Larsen J., Kristensen A.T., Hojgaard L. and Kjaer A., Simultaneous hyperpolarized ^{13}C-pyruvate MRI and ^{18}F-FDG PET (HyperPET) in 10 dogs with cancer, *J. Nucl. Med.* **56**, 2015, 1786–1792.

Haris M., Nanga R.P., Singh A., Cai K., Kogan F., Hariharan H. and Reddy R., Exchange rates of creatine kinase metabolites: feasibility of imaging creatine by chemical exchange saturation transfer MRI, *NMR Biomed.* **25**, 2012, 1305–1309.

Haris M., Singh A., Cai K., Kogan F., McGarvey J., Debrosse C., Zsido G.A., Witschey W.R., Koomalsingh K., Pilla J.J., et al., A technique for in vivo mapping of myocardial creatine kinase metabolism, *Nat. Med.* **20**, 2014, 209–214.

Henkin A.H., Cohen A.S., Dubikovskaya E.A., Park H.M., Nikitin G.F., Auzias M.G., Kazantzis M., Bertozzi C.R. and Stahl A., Real-time noninvasive imaging of fatty acid uptake in vivo, *ACS Chem. Biol.* **7**, 2012, 1884–1891.

Hill D.K., Orton M.R., Mariotti E., Boult J.K.R., Panek R., Jafar M., Parkes H.G., Jamin Y., Miniotis M.F., Al-Saffar N.M.S., et al., Model free approach to kinetic analysis of real-time hyperpolarized C-13 magnetic resonance spectroscopy data, *PLoS One* **8**, 2013, 9.

Hingorani D.V., Montano L.A., Randtke E.A., Lee Y.S., Cárdenas-Rodríguez J. and Pagel M.D., A single diamagnetic catalyCEST MRI contrast agent that detects cathepsin B enzyme activity by using a ratio of two CEST signals *Contrast Media Mol. Imaging* **11**, 2016, 130–138.

Hingorani D.V., Randtke E.A. and Pagel M.D., A catalyCEST MRI contrast agent that detects the enzyme-catalyzed creation of a covalent bond, *J. Am. Chem. Soc.* **135**, 2013, 6396–6398.

Hirsch M.L., Kalechofsky N., Belzer A., Rosay M. and Kempf J.G., Brute-force hyperpolarization for NMR and MRI, *J. Am. Chem. Soc.* **137**, 2015, 8428–8434.

Howe F.A., Barton S.J., Cudlip S.A., Stubbs M., Saunders D.E., Murphy M., Wilkins P., Opstad K.S., Doyle V.L., McLean M.A., et al., Metabolic profiles of human brain tumors using quantitative in vivo H-1 magnetic resonance spectroscopy, *Magn. Reson. Med.* **49**, 2003, 223–232.

Hu F., Chen Z., Zhang L., Shen Y., Wei L. and Min W., Vibrational imaging of glucose uptake activity in live cells and tissues by stimulated Raman scattering, *Angew. Chem. Int. Ed.* **54**, 2015, 9821–9825.

Huang C.H. and Morrow J.R., A PARACEST agent responsive to inner- and outer-sphere phosphate ester interactions for MRI applications, *J. Am. Chem. Soc.* **131**, 2009, 4206–4207.

Hurd R.E., Yen Y.F., Chen A. and Ardenkjaer-Larsen J.H., Hyperpolarized ^{13}C metabolic imaging using dissolution dynamic nuclear polarization, *J. Magn. Reson. Imaging* **36**, 2012, 1314–1328.

Iversen A.B., Busk M., Bertelsen L.B., Laustsen C., Munk O.L., Nielsen T., Wittenborn T.R., Bussink J., Lok J., Stodkilde-Jorgensen H., et al., The potential of hyperpolarized ^{13}C magnetic resonance spectroscopy to monitor the effect of combretastatin based vascular disrupting agents, *Acta Oncol.* **56**, 2017, 1626–1633.

Izquierdo-Garcia J.L., Viswanath P., Eriksson P., Cai L., Radoul M., Chaumeil M.M., Blough M., Luchman H.A., Weiss S., Cairncross J.G., et al., IDH1 mutation induces reprogramming of pyruvate metabolism, *Cancer Res.* **75**, 2015, 2999–3009.

Ji X., Bornet A., Vuichoud B., Milani J., Gajan D., Rossini A.J., Emsley L., Bodenhausen G. and Jannin S., Transportable hyperpolarized metabolites, *Nat. Commun.* **8**, 2017, 13975.

Jones K.M., Randtke E.A., Yoshimaru E.S., Howison C.M., Chalasani P., Klein R.R., Chambers S.K., Kuo P.H. and Pagel M.D., Clinical translation of tumor acidosis measurements with AcidoCEST MRI, *Mol. Imaging Biol.* **19**, 2017, 617–625.

Josan S., Hurd R., Park J.M., Yen Y.F., Watkins R., Pfefferbaum A., Spielman D. and Mayer D., Dynamic metabolic imaging of hyperpolarized [2-(13) C]pyruvate using spiral chemical shift imaging with alternating spectral ban excitation, *Magn. Reson. Med.* **71**, 2014, 2051–2058.

Karamitsos T.D., Leccisotti L., Arnold J.R., Recio-Mayoral A., Bhamra-Ariza P., Howells R.K., Searle N., Robson M.D., Rimoldi O.E., Camici P.G., et al., Relationship between regional myocardial oxygenation and perfusion in patients with coronary artery disease: insights from cardiovascular magnetic resonance and positron emission tomography, *Circ. Cardiovasc. Imaging* **3**, 2010, 32–40.

Keshari K.R., Kurhanewicz J., Bok R., Larson P.E.Z., Vigneron D.B. and Wilson D.M., Hyperpolarized ^{13}C dehydroascorbate as an endogenous redox sensor for *in vivo* metabolic imaging, *Proc. Natl. Acad. Sci. USA* **108**, 2011, 18606–18611.

Keshari K.R. and Wilson D.M., Chemistry and biochemistry of ^{13}C hyperpolarized magnetic resonance using dynamic nuclear polarization, *Chem. Soc. Rev.* **43**, 2014, 1627–1659.

Knieling F., Neufert C., Hartmann A., Claussen J., Urich A., Egger C., Vetter M., Fischer S., Pfeifer L., Hagel A., et al., Multispectral optoacoustic tomography for assessment of Crohn's disease activity, *N. Engl. J. Med.* **376**, 2017 1292–1294.

Kogan F., Haris M., Debrosse C., Singh A., Nanga R.P., Cai K., Hariharan H. and Reddy R., In vivo chemical exchange saturation transfer imaging of creatine (CrCREST) in skeletal muscle at 3T, *J. Magn. Reson. Imaging* **40**, 2014, 596–602.

Kovar J.L., Volcheck W., Sevick-Muraca E., Simpson M.A. and Olive D.M., Characterization and performance of a near-infrared 2-deoxyglucose optical imaging agent for mouse cancer models, *Anal. Biochem.* **384**, 2009, 254–262.

Kurhanewicz J., Swanson M.G., Nelson S.J. and Vigneron D.B., Combined magnetic resonance imaging and spectroscopic imaging approach to molecular imaging of prostate cancer, *J. Magn. Reson. Imaging* **16**, 2002, 451–463.

Labbé S.M., Grenier-Larouche T., Noll C., Phoenix S., Guérin B., Turcotte E.E. and Carpentier A.C., Increased myocardial uptake of dietary fatty acids linked to cardiac dysfunction in glucose-intolerant humans, *Diabetes* **61**, 2012, 2701–2710.

Lau A.Z., Miller J.J. and Tyler D.J., Mapping of intracellular pH in the in vivo rodent heart using hyperpolarized 1-13C pyruvate, *Magn. Reson. Med.* **77**, 2017, 1810–1817.

Lau J.Y.C., Chen A.P., Gu Y.P. and Cunningham C.H., Voxel-by-voxel correlations of perfusion, substrate, and metabolite signals in dynamic hyperpolarized ^{13}C imaging, *NMR Biomed.* **29**, 2016, 1038–1047.

Lee E.S. and Lee J.Y., High resolution cellular imaging with nonlinear optical infrared microscopy, *Opt. Express* **19**, 2011, 1378–1384.

Lee H.J., Zhang D., Jiang Y., Wu X., Shih P.Y., Liao C.S., Bungart B., Xu X.M., Drenan R., Bartlett E., et al., Label-free vibrational spectroscopic imaging of neuronal membrane potential, *J. Phys. Chem. Lett.* **8**, 2017, 1932–1936.

Lewis D.Y., Soloviev D. and Brindle K.M., Imaging tumor metabolism using positron emission tomography, *Cancer J.* **21**, 2015, 129–136.

Li J. and Cheng J.-X., Direct visualization of de novo lipogenesis in single living cells, *Sci. Rep.* **4**, 2014, 6807.

Li Y., Huang T., Zhang X., Zhong M., Walker N.N., He J., Berr S.S., Keller S.R. and Kundu B.K., Determination of fatty acid metabolism with dynamic [11C]palmitate positron emission tomography of mouse heart in vivo, *Mol. Imaging* **14**, 2015, 516–525.

Liu G., Li Y. and Pagel M.D., Design and characterization of a new irreversible responsive PARACEST MRI contrast agent that detects nitric oxide, *Magn. Reson. Med.* **58**, 2007, 1249–1256.

Liu G., Liang Y., Bar-Shir A., Chan K.W., Galpoththawela C.S., Bernard S.M., Tse T., Yadav N.N., Walczak P., McMahon M.T., et al., Monitoring enzyme activity using a diamagnetic chemical exchange saturation transfer magnetic resonance imaging contrast agent, *J. Am. Chem. Soc.* **133**, 2011, 16326–16329.

Liu Z., Pouli D., Alonzo C.A., Varone A., Karaliota S., Quinn K.P., Münger K., Karalis K.P. and Georgakoudi I., Mapping metabolic changes by noninvasive, multiparametric, high-resolution imaging using endogenous contrast, *Sci. Adv.* **4**, 2018, eaap9302.

Longo D.L., Bartoli A., Consolino L., Bardini P., Arena F., Schwaiger M. and Aime S., In vivo imaging of tumor metabolism and acidosis by combining PET and MRI-CEST pH imaging, *Cancer Res.* **76**, 2016, 6463–6470.

Longo D.L., Dastrù W., Digilio G., Keupp J., Langereis S., Lanzardo S., Prestigio S., Steinbach O., Terreno E., Uggeri F., et al., Iopamidol as a response MRI-chemical exchange saturation transfer contrast agent for pH mapping o kidneys: in vivo studies in mice at 7 T, *Magn. Reson. Med.* **65**, 2011, 202–211.

Longo D.L., Stefania R., Aime S. and Oraevsky A., Melanin-based contrast agents for biomedical optoacoustic imaging and theranostic applications, *Int. J. Mol. Sci.* **18**, 2017, 1719.

Longo D.L., Sun P.Z., Consolino L., Michelotti F.C., Uggeri F. and Aime S., A general MRI-CEST ratiometric approach for pH imaging: demonstration of in vivo pH mapping with iobitridol, *J. Am. Chem. Soc.* **136**, 2014, 14333–14336.

Miloushev V.Z., Granlund K.L., Boltyanskiy R., Lyashchenko S.K., DeAngelis L.M., Mellinghof I.K., Brennan C.W., Tabar V., Yang T.J., Holodny A.I., et al., Metabolic imaging of the human brain with hyperpolarized 13C pyruvate demonstrates 13C lactate production in brain tumor patients, *Cancer Res.* **78**, 2018, 3755–3760.

Mishkovsky M., Anderson B., Karlsson M., Lerche M.H., Sherry A.D., Gruetter R., Kovacs Z. and Comment A., Measuring glucose cerebral metabolism in the healthy mouse using hyperpolarized 13C magnetic resonance, *Sci. Rep.* **7**, 2017, 11719.

Mohajerani P., Tzoumas S., Rosenthal A. and Ntziachristos V., Optical and optoacoustic based tomography: theory and current challenges for deep tissue imaging of optical contrast, *IEEE Signal Process. Mag.* **32**, 2015, 88–100.

Moreno K.X., Harrison C.E., Merritt M.E., Kovacs Z., Malloy C.R. and Sherry A.D., Hyperpolarized delta-[1-(13) C]gluconolactone as a probe of the pentose phosphate pathway, *NMR Biomed.* **30**, 2017, https://doi.org/10.1002/nbm.3713.

Moreno K.X., Satapati S., DeBerardinis R.J., Burgess S.C., Malloy C.R. and Merritt M.E., Real-time detection of hepatic gluconeogenic and glycogenolytic states using hyperpolarized [2-13C]dihydroxyacetone, *J. Biol. Chem.* **289**, 2014, 35859–35867.

Muzik O., Mangner T.J., Leonard W.R., Kumar A., Janisse J. and Granneman J.G., 15O PET measurement of blood flow and oxygen consumption in cold-activated human brown fat, *J. Nucl. Med.* **54**, 2013, 523–531.

Nelson S.J., Kurhanewicz J., Vigneron D.B., Larson P.E.Z., Harzstark A.L., Ferrone M., van Criekinge M., Chang J.W., Bok R., Park I., et al., Metabolic imaging of patients with prostate cancer using hyperpolarized [1-^{13}C]pyruvate, *Sci. Transl. Med.* **5**, 2013, 198ra108.

Neves A.A. and Brindle K.M., Imaging cell death, *J. Nucl. Med.* **55**, 2014, 1–4.

Nishihara T., Yoshihara H.A., Nonaka H., Takakusagi Y., Hyodo F., Ichikawa K., Can E., Bastiaansen J.A., Takado Y., Comment A., et al., Direct monitoring of gamma-glutamyl transpeptidase activity in vivo using a hyperpolarized (13) C-labeled molecular probe, *Angew. Chem. Int. Ed.* **55**, 2016, 10626–10629.

Ntziachristos V., Going deeper than microscopy: the optical imaging frontier in biology, *Nat. Methods* **7**, 2010, 603–614.

Ntziachristos V., Tung C.H., Bremer C. and Weissleder R., Fluorescence molecular tomography resolves protease activity in vivo, *Nat. Med.* **8**, 2002, 757–760.

Osborn E.A., Kessinger C.W., Tawakol A. and Jaffer F.A., Metabolic and molecular imaging of atherosclerosis and venous thromboembolism, *J. Nucl. Med.* **58**, 2017, 871–877.

Padhani A.R., Krohn K.A., Lewis J.S. and Alber M., Imaging oxygenation of human tumours, *Eur. Radiol.* **17**, 2007, 861–872.

Pandey M.K., Bansal A. and DeGrado T.R., Fluorine-18 labeled thia fatty acids for PET imaging of fatty acid oxidation in heart and cancer, *Heart Metab.* **51**, 2011, 15–19.

Park J.M., Spielman D.M., Josan S., Jang T., Merchant M., Hurd R.E., Mayer D. and Recht L.D., Hyperpolarized ^{13}C-lactate to ^{13}C-bicarbonate ratio as a biomarker for monitoring the acute response of anti-vascular endothelial growth factor (anti-VEGF) treatment, *NMR Biomed.* **29**, 2016, 650–659.

Park J.M., Wu M., Datta K., Liu S.-C., Castillo A., Lough H., Spielman D.M. and Billingsley K.L., Hyperpolarized sodium [1-^{13}C]-glycerate as a probe for assessing glycolysis in vivo, *J. Am. Chem. Soc.* **139**, 2017, 6629–6634.

Paulus A., van Marken Lichtenbelt W., Mottaghy F.M. and Bauwens M., Brown adipose tissue and lipid metabolism imaging, *Methods* **130**, 2017, 105–113.

Perrey S. and Ferrari M., Muscle oximetry in sports science: a systematic review, *Sports Med.* **48**, 2018, 597–616.

Plathow C. and Weber W.A., Tumor cell metabolism imaging, *J. Nucl. Med.* **49**, 2008, 43S–63S.

Pleitez M.A., Hertzberg O., Bauer A., Seeger M., Lieblein T., Lilienfeld-Toal H.V. and Mäntele W., Photothermal deflectometry enhanced by total internal reflection enables non-invasive glucose monitoring in human epidermis, *Analyst* **140**, 2015, 483–488.

Pleitez M.A., Khan A.A., Reber J., Chmyrov A., Seeger M., Scheideler M., Herzig S. and Ntziachristos V., Mid-infrared optoacoustic microscopy with label-free chemical contrast in living cells and tissues, *bioRxiv* 2018, 270082, https://doi.org/10.1101/270082.

Pleitez M.A., Lieblein T., Bauer A., Hertzberg O., von Lilienfeld-Toal H. and Mäntele W., In vivo noninvasive monitoring of glucose concentration in human epidermis by mid-infrared pulsed photoacoustic spectroscopy, *Anal. Chem.* **85**, 2013, 1013–1020.

Potma E.O. and Xie X.S., Detection of single lipid bilayers with coherent anti-Stokes Raman scattering (CARS) microscopy, *J. Raman Spectrosc.* **34**, 2003, 642–650.

Raichle M.E., Bold insights, *Nature* **412**, 2001, 128–130.

Ratnakar S.J., Viswanathan S., Kovacs Z., Jindal A.K., Green K.N. and Sherry A.D., Europium(III) DOTA-tetraamide complexes as redox-active MRI sensors, *J. Am. Chem. Soc.* **134**, 2012, 5798–5800.

Reber J., Willershäuser M., Karlas A., Paul-Yuan K., Diot G., Franz D., Fromme T., Ovsepian S.V., Beziere N., Dubikovskaya E., et al., Non-invasive measurement of brown fat metabolism based on optoacoustic imaging of hemoglobin gradients, *Cell Metab.* **27**, 2018, 689–701.

Reineri F., Boi T. and Aime S., ParaHydrogen induced polarization of ^{13}C carboxylate resonance in acetate and pyruvate, *Nat. Commun.* **6**, 2015, 5858.

Rider O.J. and Tyler D.J., Clinical implications of cardiac hyperpolarized magnetic resonance imaging, *J. Cardiovasc. Magn. Reson.* **15**, 2013, 9.

Rivlin M., Tsarfaty I. and Navon G., Functional molecular imaging of tumors by chemical exchange saturation transfer MRI of 3-O-methyl-D-glucose, *Magn. Reson. Med.* **72**, 2014, 1375–1380.

Rodrigues T.B., Serrao E.M., Kennedy B.W.C., Hu D.-E., Kettunen M.I. and Brindle K.M., Magnetic resonance imaging of tumor glycolysis using hyperpolarized ^{13}C-labeled glucose, *Nat. Med.* **20**, 2014, 93–97.

Ross B.D., Radda G.K., Gadian D.G., Rocker G., Esiri M. and Falconer-Smith J., Examination of a case of suspected McArdle's syndrome by 31P nuclear magnetic resonance, *N. Engl. J. Med.* **304**, 1981, 1338–1342.

Rothman D.L., Behar K.L., Hetherington H.P., den Hollander J.A., Bendall M.R., Petroff O.A. and Shulman R.G., ^{1}H-Observe/^{13}C-decouple spectroscopic measurements of lactate and glutamate in the rat brain in vivo, *Proc. Natl. Acad. Sci. USA* **82**, 1985, 1633–1637.

Saito K., Matsumoto S., Takakusagi Y., Matsuo M., Morris H.D., Lizak M.J., Munasinghe J.P., Devasahayam N., Subramanian S., Mitchell J.B., et al., ^{13}C-MR spectroscopic imaging with hyperpolarized [1-^{13}C]pyruvate detects early response to radiotherapy in SCC tumors and HT-29 tumors, *Clin. Cancer Res.* **21**, 2015, 5073–5081.

Salamanca-Cardona L., Shah H., Poot A.J., Correa F.M., Di Gialleonardo V., Lui H., Miloushev V.Z., Granlund K.L., Tee S.S., Cross J.R., et al., In vivo imaging of glutamine metabolism to the oncometabolite 2-hydroxyglutarate in IDH1/2 mutant tumors, *Cell Metab.* **26**, 2017, 830–841.e3.

Schmidt R., Laustsen C., Dumez J.-N., Kettunen M.I., Serrao E.M., Marco-Rius I., Brindle K.M., Ardenkjaer-Larsen J.H. and Frydman L., In vivo single-shot ^{13}C spectroscopic imaging of hyperpolarized metabolites by spatiotemporal encoding, *J. Magn. Reson.* **240**, 2014, 8–15.

Schwaighofer A., Alcaráz M.R., Araman C., Goicoechea H. and Lendl B., External cavity-quantum cascade laser infrared spectroscopy for secondary structure analysis of proteins at low concentrations, *Sci. Rep.* **6**, 2016, 33556.

Serrao E.M., Kettunen M.I., Rodrigues T.B., Dzien P., Wright A.J., Gopinathan A., Gallagher F.A., Lewis D.Y., Frese K.K., Almeida J., et al., MRI with hyperpolarised [1-^{13}C]pyruvate detects advanced pancreatic preneoplasia prior to invasive disease in a mouse model, *Gut* **65**, 2016, 465–475.

Serrao E.M., Kettunen M.I., Rodrigues T.B., Lewis D.Y., Gallagher F.A., Hu D.E. and Brindle K.M., Analysis of ^{13}C and ^{14}C labeling in pyruvate and lactate in tumor and blood of lymphoma-bearing mice injected with ^{13}C- and ^{14}C-labeled pyruvate, *NMR Biomed.* 2018, e3901, https://doi.org/10.1002/nbm.3901.

Sheth V.R., Li Y., Chen L.Q., Howison C.M., Flask C.A. and Pagel M.D., Measuring in vivo tumor pHe with CEST-FISP MRI, *Magn. Reson. Med.* **67**, 2012, 760–768.

Shin P.J., Larson P.E., Uecker M., Reed G.D., Kerr A.B., Tropp J., Ohliger M.A., Nelson S.J., Pauly J.M., Lustig M., et al., Chemical shift separation with controlled aliasing for hyperpolarized (13) C metabolic imaging, *Magn. Reson. Med.* **74**, 2015, 978–989.

Shulman G.I., Rothman D.L., Jue T., Stein P., Defronzo R.A. and Shulman R.G., Quantitation of muscle glycogen-synthesis in normal subjects and subjects with non-insulin-dependent diabetes by c-13 nuclear magnetic-resonance spectroscopy, *N. Engl. J. Med.* **322**, 1990, 223–228.

Sim J.Y., Ahn C.-G., Jeong E.-J. and Kim B.K., In vivo microscopic photoacoustic spectroscopy for non-invasive glucose monitoring invulnerable to skin secretion products, *Sci. Rep.* **8**, 2018, 1059.

Sinharay S., Randtke E.A., Jones K.M., Howison C.M., Chambers S.K., Kobayashi H. and Pagel M.D., Noninvasive detection of enzyme activity in tumor models of human ovarian cancer using catalyCEST MRI, *Magn. Reson. Med.* **77**, 2017, 2005–2014.

Stoffels I., Morscher S., Helfrich I., Hillen U., Leyh J., Burton N.C., Sardella T.C.P., Claussen J., Poeppel T.D., Bachmann H.S., et al., Metastatic status of sentinel lymph nodes in melanoma determined noninvasively with multispectral optoacoustic imaging, *Sci. Transl. Med.* **7**, 2015, 317ra199.

Suchý M., Ta R., Li A.X., Wojciechowski F., Pasternak S.H., Bartha R. and Hudson R.H., A paramagnetic chemical exchange-based MRI probe metabolized by cathepsin D: design, synthesis and cellular uptake studies, *Org. Biomol. Chem.* **8**, 2010, 2560–2566.

Taruttis A., Claussen J., Razansky D. and Ntziachristos V., Motion clustering for deblurring multispectral optoacoustic tomography images of the mouse heart, *J. Biomed. Opt.* **17**, 2012, 016009.

Taruttis A. and Ntziachristos V., Advances in real-time multispectral optoacoustic imaging and its applications, *Nat. Photonics* **9**, 2015, 219–227.

Timm K.N., Hu D.-E., Williams M., Wright A.J., Kettunen M.I., Kennedy B.W.C., Larkin T.J., Dzien P., Marco-Rius I., Bohndiek S.E., et al., Assessing oxidative stress in tumors by measuring the rate of hyperpolarized [1-^{13}C]dehydroascorbic acid reduction using ^{13}C magnetic resonance spectroscopy, *J. Biol. Chem.* **292**, 2017, 1737–1748.

Togao O., Yoshiura T., Keupp J., Hiwatashi A., Yamashita K., Kikuchi K., Suzuki Y., Suzuki S.O., Iwaki T., Hata N., et al., Amide proton transfer imaging of adult diffuse gliomas: correlation with histopathological grades, *Neuro*

Oncol. **16**, 2014, 441–448.

Trokowski R., Zhang S. and Sherry A.D., Cyclen-based phenylboronate ligands and their Eu3+ complexes for sensing glucose by MRI, *Bioconjug. Chem.* **15**, 2004, 1431–1440.

Tzoumas S., Nunes A., Olefir I., Stangl S., Symvoulidis P., Glasl S., Bayer C., Multhoff G. and Ntziachristos V., Eigenspectra optoacoustic tomography achieves quantitative blood oxygenation imaging deep in tissues, *Nat. Commun.* **7**, 2016, 12121.

van Zijl P.C. and Yadav N.N., Chemical exchange saturation transfer (CEST): what is in a name and what isn't?, *Magn. Reson. Med.* **65**, 2011, 927–948.

Vander Heiden M.G. and DeBerardinis R.J., Understanding the intersections between metabolism and cancer biology, *Cell* **168**, 2017, 657–669.

Venneti S., Dunphy M.P., Zhang H., Pitter K.L., Zanzonico P., Campos C., Carlin S.D., La Rocca G., Lyashchenko S., Ploessl K., et al., Glutamine-based PET imaging facilitates enhanced metabolic evaluation of gliomas in vivo, *Sci. Transl. Med.* **7**, 2015, 274ra217.

Walker-Samuel S., Ramasawmy R., Torrealdea F., Rega M., Rajkumar V., Johnson S.P., Richardson S., Goncalves M., Parkes H.G., Arstad E., et al., In vivo imaging of glucose uptake and metabolism in tumors, *Nat. Med.* **19**, 2013, 1067–1072.

Wang J., Weygand J., Hwang K.P., Mohamed A.S., Ding Y., Fuller C.D., Lai S.Y. and Frank S.J., Magnetic resonance imaging of glucose uptake and metabolism in patients with head and neck cancer, *Sci. Rep.* **6**, 2016, 30618.

Wang J., Wright A.J., Hu D.-E., Hesketh R. and Brindle K.M., Single shot three-dimensional pulse sequence for hyperpolarized ^{13}C MRI, *Magn. Reson. Med.* **77**, 2017, 740–752.

Wang K., Zhang D., Charan K., Slipchenko M.N., Wang P., Xu C. and Cheng J.X., Time-lens based hyperspectral stimulated Raman scattering imaging and quantitative spectral analysis, *J. Biophotonics* **6**, 2013, 815–820.

Wang P., Liu B., Zhang D., Belew M.Y., Tissenbaum H.A. and Cheng J.-X., Imaging lipid metabolism in live *Caenorhabditis elegans* using fingerprint vibrations, *Angew. Chem. Int. Ed.* **53**, 2014, 11787–11792.

Ward C.S., Venkatesh H.S., Chaumeil M.M., Brandes A.H., VanCriekinge M., Dafni H., Sukumar S., Nelson S.J., Vigneron D.B., Kurhanewicz J., et al., Noninvasive detection of target modulation following phosphatidylinositol 3-kinase inhibition using hyperpolarized ^{13}C magnetic resonance spectroscopy, *Cancer Res.* **70**, 2010, 1296–1305.

Ward K.M., Aletras A.H. and Balaban R.S., A new class of contrast agents for MRI based on proton chemical exchange dependent saturation transfer (CEST), *J. Magn. Reson.* **143**, 2000, 79–87.

Wei L., Yu Y., Shen Y., Wang M.C. and Min W., Vibrational imaging of newly synthesized proteins in live cells by stimulated Raman scattering microscopy, *Proc. Natl. Acad. Sci. USA* **110**, 2013, 11226–11231.

Wieder H., Beer A.J., Holzapfel K., Henninger M., Maurer T., Schwarzenboeck S., Rummeny E.J., Eiber M. and Stollfuss J., 11C-choline PET/CT and whole-body MRI including diffusion-weighted imaging for patients with recurrent prostate cancer, *Oncotarget* **8**, 2017, 66516–66527.

Witney T.H., Kettunen M.I. and Brindle K.M., Kinetic modeling of hyperpolarized ^{13}C label exchange between pyruvate and lactate in tumor cells, *J. Biol. Chem.* **286**, 2011, 24572–24580.

Witney T.H., Kettunen M.I., Hu D.-E., Gallagher F.A., Bohndiek S.E., Napolitano R. and Brindle K.M., Detecting treatment response in a model of human breast adenocarcinoma using hyperpolarised [1-^{13}C]pyruvate and [1,4-$^{13}C_2$]fumarate, *Br. J. Cancer* **103**, 2010, 1400–1406.

Woessner D.E., Zhang S., Merritt M.E. and Sherry A.D., Numerical solution of the Bloch equations provides insights into the optimum design of PARACEST agents for MRI, *Magn. Reson. Med.* **53**, 2005, 790–799.

Wolff S.D. and Balaban R.S., Magnetization transfer contrast (MTC) and tissue water proton relaxation in vivo, *Magn. Reson. Med.* **10**, 1989, 135–144.

Wright A.J., Husson Z.M.A., Hu D.E., Callejo G., Brindle K.M. and Smith E.S.J., Increased hyperpolarized [1-13C] lactate production in a model of joint inflammation is not accompanied by tissue acidosis as assessed using hyperpolarized 13C-labelled bicarbonate, *NMR Biomed.* **31**, 2018, e3892.

Wu B., Warnock G., Zaiss M., Lin C., Chen M., Zhou Z., Mu L., Nanz D., Tuura R. and Delso G., An overview of CEST MRI for non-MR physicists, *EJNMMI Phys.* **3**, 2016, 19.

Yao J., Wang L., Yang J., Maslov K.I., Wong T.T.W., Li L., Huang C., Zou J. and Wang L.V., High-speed label-free functional photoacoustic microscopy of mouse brain in action, *Nat. Methods* **12**, 2015, 407–410.

Yoo B. and Pagel M.D., A PARACEST MRI contrast agent to detect enzyme activity, *J. Am. Chem. Soc.* **128**, 2006, 14032–14033.

Yoo B., Sheth V.R., Howison C.M., Douglas M.J., Pineda C.T., Maine E.A., Baker A.F. and Pagel M.D., Detection of in vivo enzyme activity with CatalyCEST MRI, *Magn. Reson. Med.* **71**, 2014, 1221–1230.

Zhang D., Li C., Zhang C., Slipchenko M.N., Eakins G. and Cheng J.-X., Depth-resolved mid-infrared photothermal imaging of living cells and organisms with submicrometer spatial resolution, *Sci. Adv.* **2**, 2016, e1600521.

Zhang L., Martins A.F., Zhao P., Tieu M., Esteban-Gómez D., McCandless G.T., Platas-Iglesias C. and Sherry A.D., Enantiomeric recognition of D- and L-lactate by CEST with the aid of a paramagnetic shift reagent, *J. Am. Chem. Soc.* **139**, 2017, 17431–17437.

Keywords: optoacoustic; photoacoustic; MRI; CEST; ultrasound; brown adipose tissue; lipid; blood oxygenation; diabetes; PET

Queries and Answers

Query: Have we correctly interpreted the following funding source(s) and country names you cited in your article: Cancer Research UK, United Kingdom; European Research Council, European Union; Deutsche Forschungsgemeinschaft, Germany?

Answer: Yes